A Low-cost Linkage-Spring-Tendon-Integrated Compliant Anthropomorphic Robotic Hand: MCR-Hand III

Haosen Yang[1], Guowu Wei*[2], Lei Ren*[1], Zhihui Qian[3], Kunyang Wang[3], Haohua Xiu[3], Wei Liang[3]

Abstract

This paper presents the design, analysis and development of an anthropomorphic robotic hand, i.e. MCR-Hand III. Based on the investigation of human hand anatomical structure and the related existing robotic hands, mechanical design of the MCR-Hand III is presented, and a detailed introduction for mechanical compliance of the hand, which is achieved through the combinations of springs with four-bar 4R linkages and tendons, is provided. Using D-H convention, kinematics and force analysis of the hand are formulated and illustrated with numerical simulations, laying background for comparison and evaluation. Subsequently, prototype of the proposed robotic hand is developed, and fingertip force calibration and validation are conducted. Further, a three-stage algorithm for object stiffness identification and adaptive grasping is proposed and evaluated, and grasping evaluation based on Cutkosky taxonomy with additional deformable object lifting operation and piano manipulation is carried out. The proposed MCR-Hand III costs less than $800 and is hence affordable for wider applications. The experimental results indicate that the proposed hands are capable of implementing the grasp and manipulation for most of the objects used in daily life.

Keywords: Robotic hand, anthropomorphic hand, linkage-tendon-hybrid-driven, mechanical compliance, object stiffness identification

1. Introduction

The human hand is the most dexterous known end-effector, consisting of 29 joints and 27 bones. It can be considered as the crucial organ for exploration and adaptation of the external environment for the human being. It plays a vital role in human's perception, prehension and manipulation in daily life tasks. Because of its complexity, building an artificial hand capable of replicating the functionalities of the human hand remains one of the biggest challenges in robotics. 'Berlichingen hand' in the 16th century could be seen as the first attempt of the design and development of the functional robotic hand and it has been over a half-century since the modern research in robotic hand emerged [1]. Over the years, several design methods and prototypes have been proposed. A rather comprehensive review on the design of robotic hand in the past century was recently presented by Piazza et al. [2].

In the development of early robotic hands, due to the limitation of actuator and manufacturing process, the robotic hands were simplified into grippers with specific functions for industrial applications [3]. In addition, early anthropomorphic robotic hands were simplified in both structure

*Corresponding authors

Email addresses: haosen.yang@postgrad.manchester.ac.uk (Haosen Yang), g.wei@salford.ac.uk (Guowu Wei*), lei.ren@manchester.ac.uk (Lei Ren*), zhqian@jlu.edu.cn (Zhihui Qian), kywang@jlu.edu.cn (Kunyang Wang), xiuhh@jlu.edu.cn (Haohua Xiu), weiliang16@mails.jlu.edu.cn (Wei Liang)

[1]School of Mechanical, Aerospace and Civil Engineering, The University of Manchester, Manchester M13 9PL, United Kingdom

[2]School of Science, Engineering and Environment, University of Salford, Salford M5 4WT, United Kingdom

[3]Key Laboratory of Bionic Engineering, Ministry of Education, Jilin University, Changchun 130025, China

and function, providing grasping functions for prosthetic use such as the Belgrade hand [4, 1]. The Okada hand [5] and the later on Utah/MIT hand [6] were considered as the cornerstone for design and development of dexterous robotic hands. After that, researchers have continuously been improving the design strategy of robotic hands in both structure and control methods[2]. One of the trends in dexterous robotic hand research is to develop anthropomorphic robotic hands that can closely mimic the salient biological features of the human hand, aiming at being able to perform complex tasks and manipulations. Such anthropomorphic robotic hands include, to mention but a few, the Hitachi Hand [7], the DIST hand [8], the DLR Hand I and II [9, 10], the Robonaut 1 and 2 hands [11, 12], the Metamorphic hand [13, 14, 15], and the Shadow Hand®. In the design of these anthropomorphic robotic hands including the underactuated hands [16, 17] (except for the recent development of soft-material-based anthropomorphic robotic hands [18, 19, 20], which provide better adaptability for dexterous grasping but lack of full versatile in-hand manipulability comparing to human hand), a variety of transmission systems including linkages, tendons, gear trains and belts were used. Among these driven systems, the tendon and linkage systems are the two transmissions system that have been mostly implemented. The tendon-driven robotic hands normally use remotely located actuators for the purpose of providing better inertia property with higher power; it can also reduce the weight and dimensions of the robotic hands. The well-known tendon-driven anthropomorphic robotic hands are the Stanford/JPL hand [21], the Utah/MIT hand [6], the Shadow Hand®, the ACT hand [22] and the DEXMART hand [23]. The linkage-driven robotic hands can provide accuracy in control and allow bidirectional control. On the other hand, it also limits the size of the actuators and increases the weight and dimensions of the phalanges. Typical linkage-driven anthropomorphic robotic hands are the Gifu hand III [24], the NAIST Hand [25] and the Robonaut 2 hand [12]. In addition to these, robotic hand using fewer actuators with opportunely designed tendon-driven differential mechanism was also recently developed [26, 27].

In human hand grasp, it is found that the passive behaviour of the human body due to the parallel and series compliance helps human hand achieve better and stable performance [28]. Inspired by human body, robotic systems and hands with variable stiffness/compliance have been designed and developed. Such design and development were mainly achieved through the construction of compliant actuators [29, 30, 31] and the introduction of stiffness variable joints [32, 33]. It has been shown that robotic hand with variable stiffness or compliance could improve stability and simplify control during grasp and manipulation [34, 35]. However, mechanical compliance realized through the transmission systems in robotic design has rarely been reported.

Further, it has been noticed that except for some prosthetic hands [36, 37], most of the anthropomorphic robotic hands are expensive due to the high costs of component fabrication, actuators, and sensory and control systems, and thus applications of these robotic hands are limited. The emerging 3D printing technology has made the design and development of robotic hand convenient and affordable. Using such rapid prototyping technology, a great number of robotic hands have been presented [23, 17, 38], and a number of open-source initiatives such as the Open Hand Project [39] and the OpenBionics platform [40] were established for supporting such a development.

From the literature, we noticed that in most of the cases either tendon-driven or linkage-driven method was implemented in the design of most rigid-body-based anthropomorphic robotic hands, hence these hands either have remotely located actuators or are too big in size. In this paper, we aim to design a low-cost 3D-printed anthropomorphic robotic hand by using a linkage and tendon combined transmission system, low-cost servomotors with sufficient driving power are used as actuators integrated with economical sensors and micro-controllers. In addition, mechanical compliance through the transmission systems is introduced in the hand design, which is achieved by integrating springs with linkage-driven and tendon-driven systems. It is expected that: 1) the proposed hand is approximately in the size of an adult human hand; 2) each finger and the thumb can generate up to 7N controllable fingertip force (to be validated by experiment); 3) the overall weight of the hand is within 500g by applying 3D printing technology (excluding power supply); and 4) is under an affordable cost, less than $800 ($600 for material cost including motors, sensors, controllers, and other mechanical and electronic components, $200 for 3D printing cost). Hence, compared with the existing robotic hands, this paper presents a full-functional affordable linkage-and-tendon hybrid-driven anthropomorphic robotic hand with mechanical compliance for better grasping and manipulation. It is suitable for lightweight robotic system integration with potential applications in the fields such as fruit and food processing, human-robot interaction, and autonomous product assembly.

The rest of this paper is organized as follows. Section 2 describes the mechanical design of the MCR-Hand III including the compliant transmission system design, and Section 3 presents kinematics and force analysis of the robotic hand which covers workspace, manipulability and fingertip force analysis. Then, prototype, electronics, sensory and control systems are addressed and explained in Section 4 with the focus on an approach for object stiffness identification and smart grasping. Section 5 presents empirical study and evaluation of the proposed robotic hand, and brief conclusions with results achieved in this paper are drawn in Section 6.

2. Mechanical Design of the MCR-Hand III

Figure 1 shows mechanical structure of the MCR-hand III, it contains five fingers and a split articulated palm (the distribution of degrees of freedom will be shown in Figure 5). All the digits have four degrees of freedom which are actuated by three servo motors through linkage-and-tendon hybrid transmission systems. The palm is split into two sections along joint axis PL, as indicated in Fig. 1 (a) and (b), providing flex for the ring and little fingers. Joint PL is actuated by a servo motor SM-P/F through a four-bar linkage denoted as "Linkage P/F". The detailed structure for actuating the split palm is illustrated in Fig. 1(c), there is a dual-spring system inside the linkage P/F to absorb axial load from both sides, providing compliance for the palm. In this design, the robotic hand is driven by totally 16 four-bar 4R linkages and five tendons associated with return springs (elastic wires). This is a robotic hand with twenty-one degrees of freedom that is driven by sixteen actuators.

Linkage-and-tendon hybrid transmission systems and modular design scheme are used in the design of the MCR-hand III. The advantage of such design is the compact size of the proposed robotic hand, actuators for the PIP/DIP (IP/MCP for the thumb) joints are located inside the proximal phalanges, and actuators for the MCP (CMC) joints are located inside the palm. Hence, there is no need for a forearm to accommodating the actuators and electronic components. In this design, since the actuating for MCP and PIP/DIP joints are independent, the problems caused by mutual influence in the traditional tendon-driven robotic hand can be eliminated. In addition, the modular design makes the assembly and maintenance of the proposed robotic hand convenient, each finger is independent of the other fingers and the palm. Further, in order to provide the finger joints compliance, springs are used integrating with the traditional four-bar linkages and the tendons, leading to the compliant linkage and tendon transmission systems which will be detailed in the following sections. Moreover, in order to reduce friction, ball bearings are used in all the finger joints.

Further, by adapting the data from cadaver hands [41] size of the proposed robotic hand is close to an adult male hand (the hand length was described as the distance from the distal wrist crease to the tip of the long finger with the hand in full extension). In the proposed design, the overall length and width of the robotic hand are about 205mm and 110mm, respectively, and the thickness is about 34mm. Dimensions of phalanges in the robotic hand are listed in Table 1.

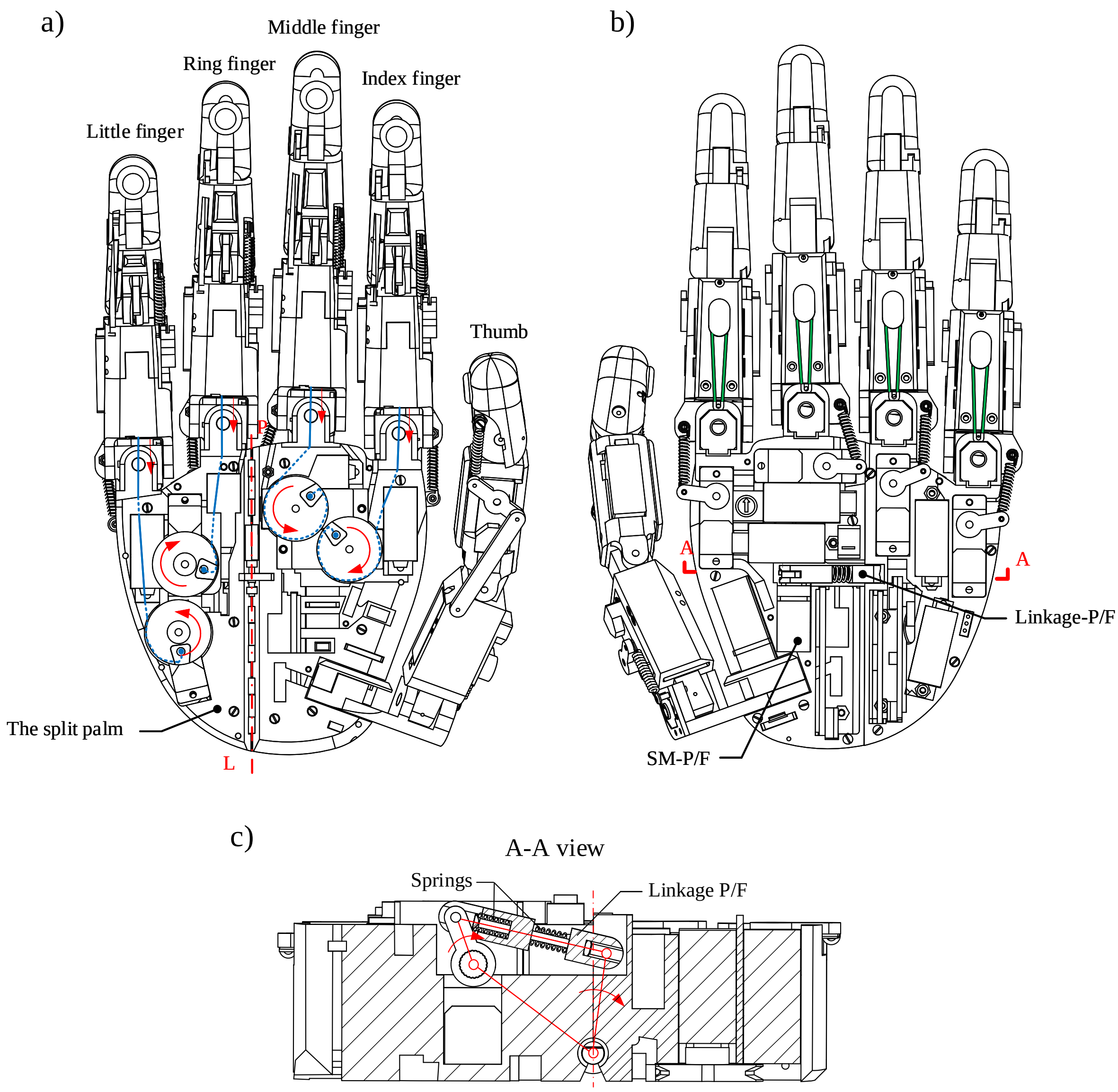

Figure 1: The mechanical structure of the MCR-Hand III. a) The front view: the blue line represents the routine of the tendon that drives the MCP-1 joint, partially through the palm; the red arrow on the palm indicates the direction in which the reel rotates when the MCP-1 joint flex. b) The rear view: the palm is split into two sections along joint axis PL. c) The A-A section view: the right palm can be driven by the motor through the linkage P/F to form an angle with the left palm; dual-spring linkage P/F can provide compliance for the palm.

2.1. The Compliant Linkage-and-Tendon Driven Robotic Finger

Modular design approach is implemented in the design of the MCR-hand III. The index, middle, ring and little fingers share the same type of module whose detailed mechanical structure is illustrated in Fig. 2(a). This finger module contains three phalanges including the proximal, middle and distal phalanges, and three joints including a 1-DoF DIP (distal interphalangeal) joint, a 1-DoF PIP (proximal interphalangeal) joint, and a 2-DoF MCP (metacarpophalangeal) joint, which is denoted as MCP-1 and MCP-2 respectively forming a universal joint. The proximal phalanx of the finger is composed of two separable parts (see Fig. 2 (b)). The electronic components and motors inside the middle and distal phalanges of the finger are connected to the palm through the male and female connectors above the proximal phalanx. The separated proximal phalanx can be connected to the upper fixing plate by screws (see Fig. 2 (a)). In order to mimic the function of human finger, motion of the DIP joint is coupled with that of the PIP joint through a four-bar linkage, denoted as DIP coupling linkage as shown in Fig. 2(a). The four-bar mechanism allows the maximum joint angle of DIP to be about 80% of that of the PIP joint [42, 43, 44]. In order to

Table 1: Lengths of phalanges in the MCR-Hand III (in mm)

Digit	Proximal	Middle	Distal	Total length
Index	53.31	28.28	18.85	100.44
Middle	57.30	32.28	18.73	108.31
Ring	53.50	29.28	18.78	101.56
Little	52.32	22.28	18.79	93.39
Thumb	Metacarpal	Proximal	Distal	
	46.41	49.39	21.75	117.55

embed the motor in the finger, another four-bar linkage denoted as PIP driving spring linkage is used to transmit torque from Motor 1 to the PIP joint.

The MCP-1 joint is a tendon-driven joint, with the tendon indicated in blue line in the figure, one end of the cable is connected at the end of a linear spring that is fixed inside the proximal phalanx, and the other end of the cable is connected to the pulley mounted on Motor 3. The tendon provides one-direction actuation for the flexion of the MCP joint, and the extension of MCP joint is achieved by the passive elastic wire as indicated in green in the figure, which simplifies tendon routing and therefore reduce number of actuators. In addition, the adduction and abduction of the MCP joint, i.e. MCP-2 is actuated through a third four-bar linkage, denoted as MCP-2 driving spring linkage, driven by a servo Motor 2. Position sensors are embedded on the joints and fingertip force sensor is mounted inside the pad of distal phalanx with the detailed structure illustrated in Fig. 2(a). All the linkages used for the transmission are link-spring integrated compliant linkages.

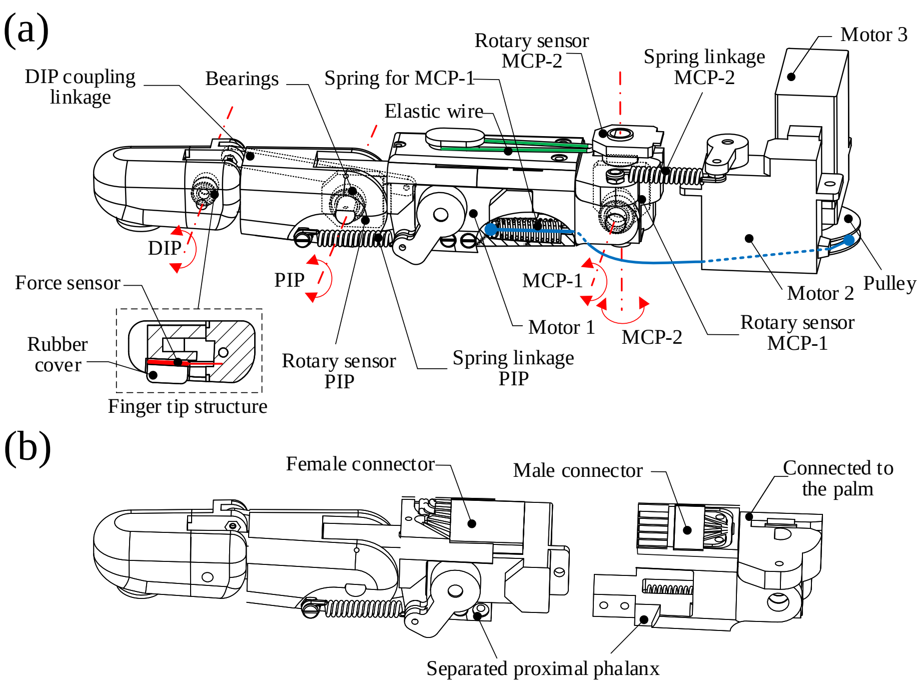

Figure 2: a) The mechanical structure of the fingers, including the index, middle, ring and little fingers. Each finger includes a 2-DOF MCP joint, a 1-DOF PIP joint and a 1-DOF DIP joint. PIP joint and MCP-2 joint are driven by motor 1 and motor 2 though spring linkages. DIP joint is coupled with PIP joint thought coupling linkage. MCP-1 joint is driven by motor 1 through tendon, and the extension is achieved by the elastic wire. The cross-section of the proximal phalange of the finger is used to show the tendon-spring system of the MCP-1 joint in detail. Rotary sensors are used in each joint excluding DIP joint. b) The finger separated from the palm by the separated proximal phalanx.

Further, mechanical structure of the thumb module is shown in Fig. 3. It contains a distal phalanx, a proximal phalanx and a metacarpal bone, connected by the IP joint, MCP joint and a 2-DoF CMC joint. The IP joint is coupled with the MCP joint, driven by one motor (Motor 1) through two compliant four-bar linkages denoted as “IP joint linkage" and “MCP joint linkage", respectively. The CMC-2 joint is actuated by Motor 2 through another compliant four-bar linkage denoted as “CMC-2 joint linkage". And the CMC-1 joint is directly driven by Motor 3 through a resilient coupling system indicated in Fig. 3(c). The resilient coupler is composed of an input coupling, an output coupling, a torsion spring, and bearings. Similar to the fingers, the thumb can also be separated from the palm of the robotic hand through the separated proximal phalanx (see Fig. 3 (d)).

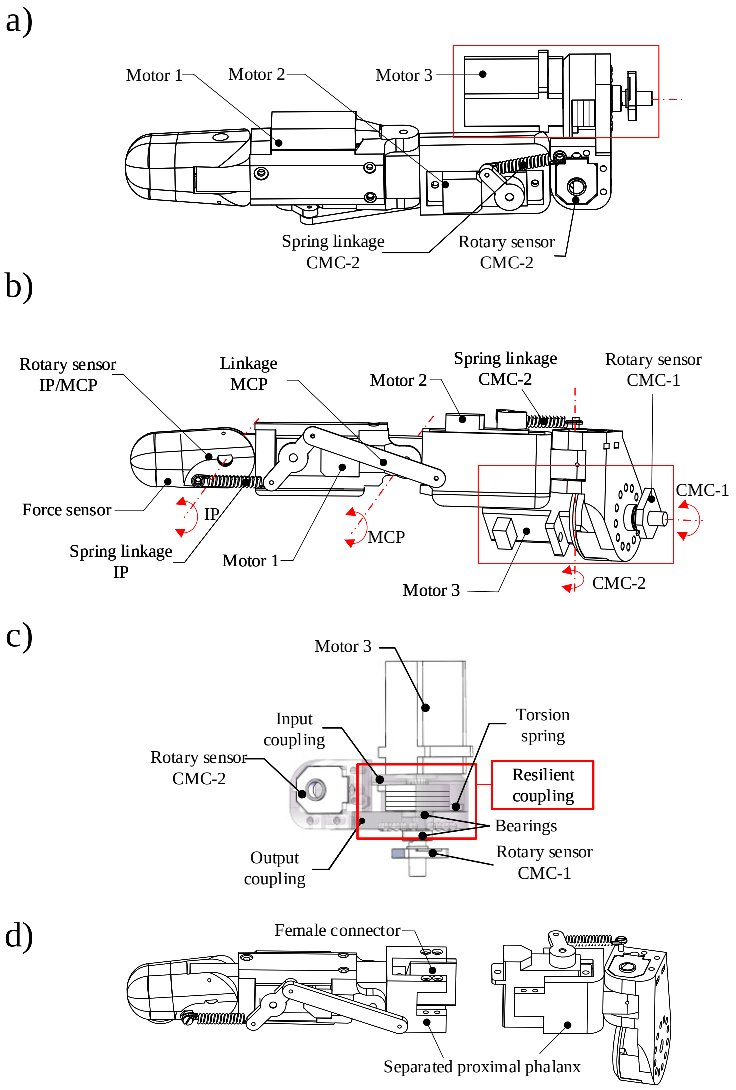

Figure 3: The mechanical structure of the thumb. a) side view, b) rear view, and c) resilient coupling system for the CMC joint. d) The finger separated from the palm by the separated proximal phalanx. The thumb including a 2-DOF CMC joint, a 1-DOF MCP joint and a 1-DOF IP joint. CMC-2 and IP joint are driven by motor 1 and motor 2 through spring linkages. CMC-1 joint is directly driven by motor 3 thought the resilient coupling system.

2.2. The LST and TST Compliant Transmission Systems

In the finger and palm design, in order to introduce mechanical compliance, as shown in Figs. 2 and 3, the coupler link in the traditional four-bar linkage is replaced by a linear spring such that the linkage becomes a link-spring-integrated four-bar four-R (R stands for revolute joint) linkage, or simply a compliant four-bar linkage. In such a linkage, the motor rotation angle and joint angle can still be deduced using the classical 4R linkage transmission equations. By replacing the coupler link with an linear spring, it introduces a new variable for the equations, i.e deformation of the coupler link and thus the variable joint torque of the output link. Since the linear spring is used and integrated in the linkage driven system, we call this system linkage-spring-transmission (LST) system.

In addition, in order to implement mechanical compliance on the tendon-driven joints, linear springs are attached to the tendons, as shown in the design of MCP-1 joint in the fingers indicated in Fig. 2(a), and we call this system tendon-spring-transmission (TST) system.

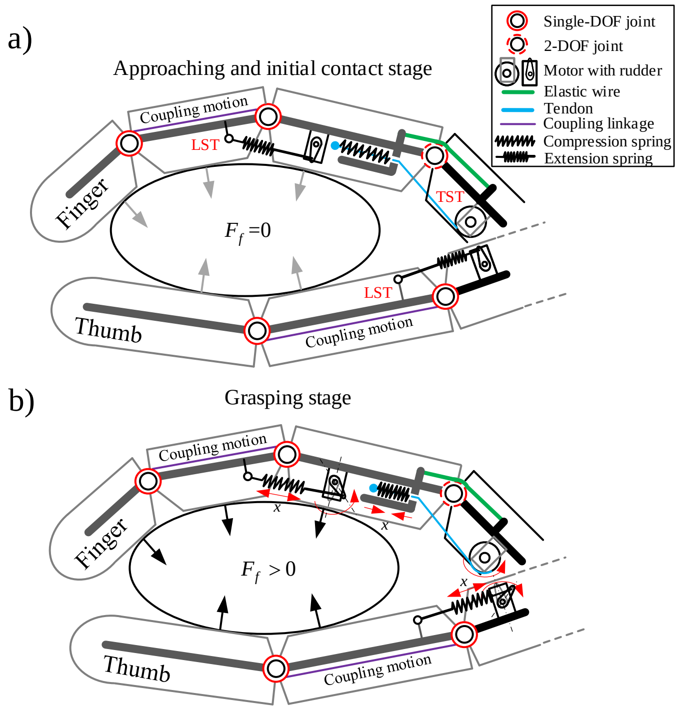

Figure 4: Working principle of the LST and TST systems in the hand. a) The finger approaching and initial contact stage, b) grasping stage.

Figure 4 illustrates the working principle of the LST and TST systems. They work in two stages, i.e. the approaching and initial contact stage and the grasping stage. In the approaching and initial contact stage, the finger surface contact the object but no contact force is generated, and hence at this stage the four-bar linkages and the tendon-driven systems work like the traditional ones. When the joints rotate further, joint rotation is restricted and it enters the grasping stage. In this stage, when the joints continues to rotate, the tension spring in the LST system is stretched, and in the TST system the compression spring is compressed; and thus the joint torque increases and a contact force is generated.

The LST and TST transmission systems introduced mechanical compliance and thus variable joint torque in the mechanical design, which makes joint torque control easier and more accurate. For the LST and TST structures, there are relations among the joint torque, finger joint angle and its associated servo joint angle. These relations are to be addressed in detail in Section 3.3. Further, it can be shown in Section 4 that by using the LST and TST systems, a single grasping synergy can be used to grasp objects of different shapes and stiffness.

In addition, the introduction of mechanical compliance helps improve hardware safety. Some robotic hands use sensors to detect unexpected external forces to protect the hardware, which requires advance algorithms and high response speeds. However, in the proposed LST and TST systems, by adding the springs to the structures as filters, unexpected external forces can be directly absorbed by the springs, thereby achieving hardware safety.

3. Kinematics and Force Analysis

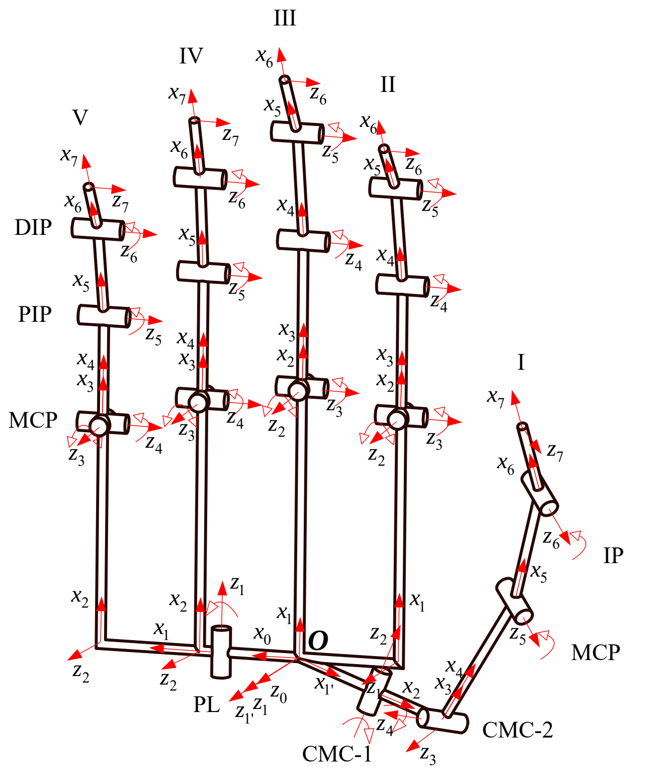

Figure 5: Schematic structure and coordinate systems of MCR-hand III. MCP: Metacarpophalangeal joint, PIP: Proximal interphalangeal joint, DIP: Distal interphalangeal joint, PL: Palm joint, CMC: Carpometacarpal joint, IP: Interphalangeal joint.

Schematic structure of the proposed MCR-hand III is illustrated in Fig. 5. The digits are numbered I, II, III, IV and V from the right to left corresponding to the thumb, and the index, middle, ring and little fingers. All the digits have four degrees of freedom, and the palm provides a flex for the ring and little fingers about axis PL. According to the D-H convention [45], coordinate frames are attached to the joints and fingertips of the hand as shown in the figure. Joint angles are denoted as θ_{ij} with subscripts i =1, 2, 3, 4 and 5 corresponding to number of the digits and j standing for the joint number in each individual digit. Joint angles for the DIP (IP) joints are coupled with that of the PIP(MCP) joints, and the other joints in the hand are independently actuated. Based on the geometry shown in Fig. 5, kinematics and force analysis of the hand are studied in this section.

3.1. Kinematics of the Linkages in MCR-Hand III

The present MCR-Hand III is a linkage and tendon hybrid driven anthropomorphic robotic hand. Linkages are used in design of the digits and splitting palm. The four-bar 4R linkages are used in coupling the rotation between DIP and PIP joints in the fingers (IP and MCP joints in the thumb), and in driving the PIP and MCP-2 joints in the fingers, the MCP, CMC-2 joints in the thumb and the splitting joint in the palm.

Considering all the four-bar 4R linkages in the hand, let the driving joint be labelled as D, the driven joint as A, and the two joints on the coupler as B and C with B adjacent to A and C next to D. Lengths of links AD, AB, BC and CD are denoted as l_0, l_1, l_2, and l_3, respectively. Further, let the driving joint angle associated with joint A be θ_1 and the driven joint angle at joint D be θ_3, based on the classical formulation for a four-bar-4R linkage, the relation between θ_1 and θ_3 can be obtained as:

$$\theta_3 = f_1(\theta_1) = 2\arctan\left(\frac{B \pm \sqrt{A^2 + B^2 + C^2}}{A - C}\right) \quad (1)$$

With $A = l_0 - l_1\cos\theta_1$, $B = -l_1\sin\theta_1$ and $C = (A^2 + B^2 + l_3^2 - l_2^2)/2l_3$.

Due to rotation limitation of the servo motors, only the positive solution is valid. Once the angle θ_3 is obtained, the coupler joint θ_2 can be derived as

$$\theta_2 = \arctan\left(\frac{B + l_3\sin\theta_3}{A + l_3\cos\theta_3}\right) \tag{2}$$

Using these equations, the linkage-driven joint angles in the fingers can be explicitly obtained by given the servo joint angles.

3.2. Finger and Thumb Kinematics

All fingers have the same kinematic structure and the thumb has a slightly different one. In this subsection, the kinematic of the fingers will be analysed. The coupled joints PIP/DIP will be first calculated, followed by the workspace analysis of fingers and the hand.

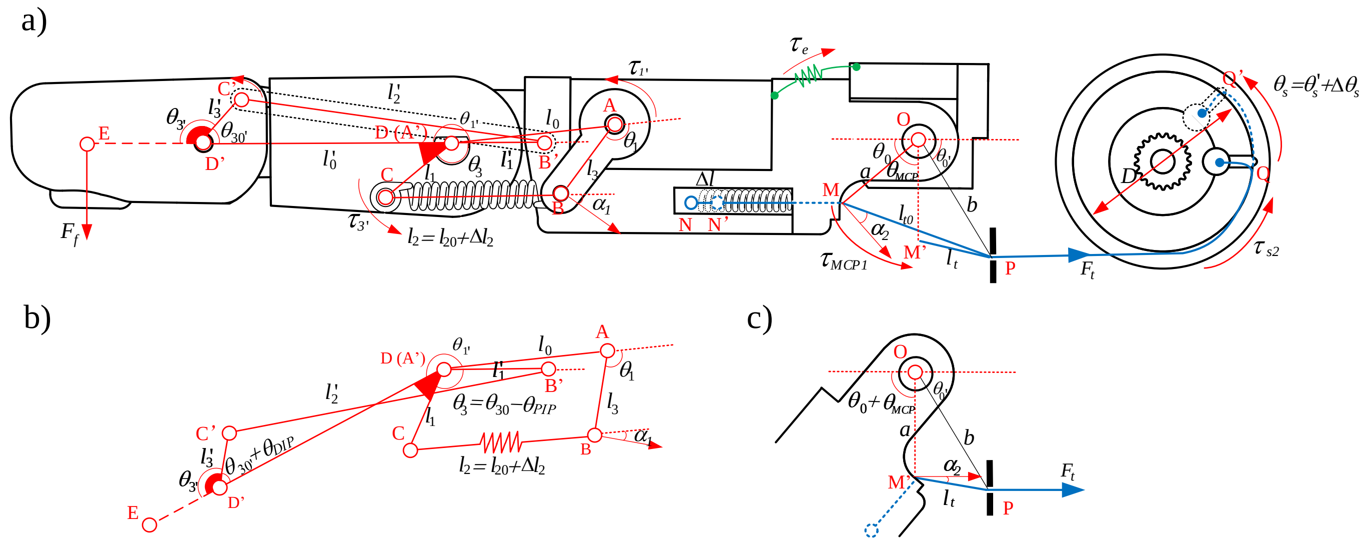

Figure 6: Structure, geometry, force and torque in a finger. a) four-bar 4R linkages systems in DIP/PIP joint and Tendon-Spring system in MCP-1 joint when the finger is in full extension. The solid part indicates the consolidation between the linkages. In this case, $\theta_{PIP} = 0$, $\theta_{DIP} = 0$, N-M-P-Q represents the path and position of tendon when θ_{MCP}=0, N'-M'-P-Q' represents the path and position of tendon when $\theta_{MCP} > 0$ and $F_t > 0$. b) four-bar 4R linkage systems in DIP/PIP joint when flexion and force applied on fingertip, where $\theta_{PIP} > 0$, $\theta_{DIP} > 0$, $\Delta l_2 > 0$. c) tendon-spring system in MCP-1 joint when finger flexion, where $\theta_{MCP} > 0$.

For the fingers designed in the MCR-hand III, the DIP joint angle θ_{DIP} is coupled with the PIP joint angle θ_{PIP}. As shown in Fig. 6(a), which gives the natural and initial configuration of a finger, geometry of the linkages and angles are presented. In the four-bar 4R linkage (A-B-C-D), the input angle of the linkage is θ_1, hence, using the general relation in Eq. (1), according to Fig. 6(b), rotation angle of the PIP joint is

$$\theta_{PIP} = \theta_{30} - \theta_3 = \theta_{30} - f_1(\theta_1) \tag{3}$$

where θ_{30} is the initial angle of θ_3. θ_{PIP} can be expressed by the rotation angle of linkage DC or linkage A'D'.

Thus the input angle $\theta_{1'}$ in linkage A'-B'-C'-D' can be deduced from Fig. 6(b) as

$$\theta_{1'} = \theta_{PIP} + \pi \tag{4}$$

Then in linkage A'-B'-C'-D', angle $\theta_{3'}$ can be obtained by using Eq. (1) as

$$\theta_{3'} = f_1(\theta_{1'}) \tag{5}$$

and thus from Fig. 6(b), joint angle of the DIP joint can be deduced as

$$\theta_{DIP} = \pi - \theta_{3'} - \theta_{30'} \tag{6}$$

where angle $\theta_{30'}$ equals the value of angle $\angle A'D'C'$ at the initial configuration of the finger which is indicated in Fig. 6(a).

Hence, from the above derivation the DIP joint angle is coupled with the PIP joint angle.

Referring to Fig. 5, the angles θ_{PIP} and θ_{DIP} correspond to joint angles θ_{i4} and θ_{i5}, respectively for the index and middle fingers with $i = 2$ and 3, and to joint angles θ_{i5} and θ_{i6} respectively for the ring and little fingers with $i = 4$ and 5. Further, extension and flexion of the MCP joint is independently driven by tendon which is denoted by angle θ_{i3} for the index and middle fingers, and θ_{i4} for the ring and little fingers. Adduction and abduction of the MCP joint is separately driven by another four-bar linkage given by angle θ_{i2} for the index and middle fingers, and θ_{i3} for the ring and little fingers.

Considering the thumb, the IP joint is coupled with the MCP joint, such that angle θ_{16} can be related to angle θ_{15} by using Eq. (1) similar to the derivations shown in Eq. (2) to Eq. (5). The CMC-1 joint is driven directly by a motor and CMC-2 is driven through a four-bar linkage. Joint angles for these two joints are given as θ_{12} and θ_{14}, respectively.

Then based on the D-H parameters (see Appendix A) obtained according to the coordinate frames in Fig. 5, postures of the tips of the fingers and thumb can be obtained as:

$$\mathbf{T}^0_{ni} = \mathbf{T}^0_{1i}\mathbf{T}^1_{2i}\ldots\mathbf{T}^{n-1}_{ni} \tag{7}$$

where the matrix $\mathbf{T}^k_{ji} = \left(\boldsymbol{p}^k_{ji}, \mathbf{R}^k_{ji}\right) \in SE(3)$ is the homogeneous matrix giving both position and orientation of frame j with respect to frame k, with i denoting the finger number. n is the number of frames associated to finger i: for the thumb, $n = 7$; for the index and middle finger, $n = 6$; and for the ring and little fingers, $n = 7$. Using Eq. (7), workspace of the fingers and thumb can be computed.

Following Eq. (7), Jacobian [46] of each finger can be formulated as

$$\mathbf{J} = \begin{cases} [\boldsymbol{J}_{21}\ \boldsymbol{J}_{41}\ \boldsymbol{J}_{51}], & \text{for thumb } (i=1) \\ [\boldsymbol{J}_{2i}\ \boldsymbol{J}_{3i}\ \boldsymbol{J}_{4i}], & \text{for index and middle finger } (i=2,3) \\ [\boldsymbol{J}_{1i}\ \boldsymbol{J}_{3i}\ \boldsymbol{J}_{4i}\ \boldsymbol{J}_{5i}], & \text{for ring and little finger } (i=4,5) \end{cases} \tag{8}$$

where $\boldsymbol{J}_{ji} = \begin{bmatrix} \boldsymbol{z}^0_{ji} \times \left(\boldsymbol{p}^0_{ni} - \boldsymbol{p}^0_{ji}\right) \\ \boldsymbol{z}^0_{ji} \end{bmatrix}_{6\times 1}$ with $\boldsymbol{z}^0_{ji}$ being a unit vector along the axis of joint ji (j stands for the joint number, and i for the finger number) expressed in the base frame {0}, which can be derived as $\boldsymbol{z}^0_{ji} = \mathbf{R}^0_{1i}\mathbf{R}^1_{2i}\ldots\mathbf{R}^{j-1}_{ji}\boldsymbol{z}_0$ given $\boldsymbol{z}_0 = [\ 0\ \ 0\ \ 1\ ]^T$. The terms $\boldsymbol{p}^0_{ni}$ and $\boldsymbol{p}^0_{ji}$ are position vectors of the fingertip and frame j, respectively in finger number i, expressed in the base frame {0}. It should be pointed out that the terms $\boldsymbol{J}_{51}$, $\boldsymbol{J}_{4i}$ and $\boldsymbol{J}_{5i}$ in Eq. (8) carry kinematic information for both the coupled DIP and PIP joints in the fingers and thumb.

From the Jacobian formulated above, manipulability [47] of the fingers and thumb, which predicts the dexterity to move and apply forces in arbitrary directions, can be derived and expressed in Frobenius norm form as

$$w = \frac{1}{\|\mathbf{J}\|_F}, \text{ with } \|\mathbf{J}\|_F = \sqrt{\frac{1}{m} tr\left(\mathbf{J}\mathbf{J}^T\right)} \tag{9}$$

Table 2: Motion range of the joints in the digits (in °)

Joint	Index	Middle	Ring	Little	Thumb
MCP-1/CMC-1	0-90	0-90	0-90	0-90	0-90
	(−22-83)	(−22-90)	(−23-88)	(−34-90)	(0-53)
MCP-2/CMC-2	−30-0	−25-25	0-30	0-30	0-90
	(−21-21)	(−20-20)	(−21-21)	(−24-24)	(0-42)
PIP/MCP	0-97	0-97	0-97	0-97	0-90
	(−10-101)	(−11-103)	(−12-105)	(−7-103)	(0-45)
DIP/IP	0-81	0-81	0-81	0-81	0-81
	(−11-73)	(−11-80)	(−12-75)	(−12-78)	(0-100)

The data shown in parentheses is for the human hand, all the data is collected from [48, 49, 50] and rounded. Data for the thumb are only the overall range of motion.

where $tr\left(\mathbf{JJ}^T\right)$ is the trace of matrix $\mathbf{JJ}^T$, and m denotes degrees of freedom of the finger.

By carefully assigning the link lengths of the four-bar linkages according to the sizes of the phalanges listed in Table 1 and using Eq. (1), the rotation ranges of the finger joints are obtained and listed in Table 2. Additionally, the rotation range of the palm splitting joint PL is $0° - 55.5°$ driven by a servo motor of rotation range $0° - 44.9°$.

Then using the kinematic analysis results obtained above, and range of motion for the joints presented in Table 2, workspace and manipulability of the digits can be computed and illustrated as shown in Fig. 7. The colour of the point represents the value of manipulability w in this point (close to red means better manipulability, w close to 1; close to black means less manipulability, w close to 0).

From the figure, it can be seen that workspace of the ring finger is larger than that of the one with a rigid palm: workspace for ring finger with a splitting palm is 500 cm^3, while that of the rigid palm is 184 cm^3, about 270 % greater. In addition, workspace of the little finger is 316% larger than that of one with rigid palm. Manipulability of the hand is very close with that of a human hand.

3.3. *Finger Force Analysis*

Mechanical compliance is introduced in the MCR-hand III, and all the joints are driven by either linkage-spring-integrated (LST) or tendon-spring-integrated (TST) transmission systems such that the joint torques are controllable. This feature is important in grasping soft objects and manipulating fragile objects. In this section, the relation between joint angle, motor rotation angle, and joint torque for the fingers will be deduced. The relations are useful for detecting contacting and realizing fingertip force control in Section 4.3. It should be noted that friction from the driving tendon of is affected by complex facts, such as printing materials, printing accuracy, tendon material, changes in tendon guide holes, load, and tendon wear status. These factors are difficult to quantify, and hence friction is not considered in the mathematical model. However, in the design process of the robotic hand, we try to ensure that tendon is tangent to the guide hole and to direction change of the guide hole is minimum. In addition, the use of bearings in each joint further reduces friction.

3.3.1. *Torque analysis for the LST system*

The transmission system of the proposed MCR-hand III is achieved through the combination of linkage and tendon driven system integrated with springs which introduces mechanical compliance. Hence, the forces and torques in the hand need to be calculated in two stages, i.e. one stage that the springs are not in action, and the other stage that the springs are in action.

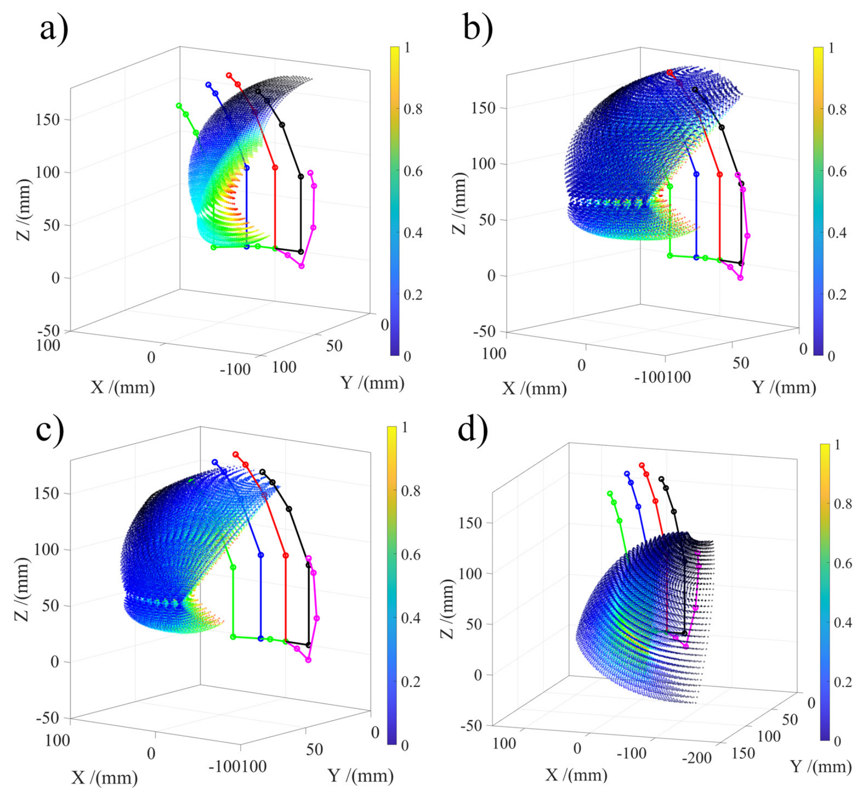

Figure 7: Workspace and manipulability for the fingers and thumb. a) the index finger, b) the ring finger, c) the little finger, d) the thumb. The colour of the point represents the value of manipulability w in this point (close to red means better manipulability, w close to 1, close to black means less manipulability, w close to 0).

For the linkage-spring-transmission (LST) system, we investigate the torque transmission by taking the linkage in the PIP joint as shown in Fig. 6(a) as an example. In the stage that the springs are not in action, corresponding to the approaching and initial contact stage describe in Section 2.2, based on the same joint and structure parameter assumptions proposed for Eq. (1), the output torque (associated with the driven joint angle θ_3) in a four-bar linkage can be represented by the input torque (i.e. torque from the servo) which is associated with the driving angle θ_1 as

$$\tau_3 = f_2(\tau_1) = \frac{l_3 \sin(\theta_3 - \theta_2)}{l_1 \sin(\theta_1 - \theta_2)} \tau_1 \tag{10}$$

where angles θ_2 and θ_3 are formulated in Eq. (1).

In the stage that the springs (mechanical compliance) are in action (see Fig. 6 (b)), when the hand exert forces on object for grasping and manipulation, the output torque needs to be calculated by considering deformation of the spring, which acts as the coupler link in the four-bar linkage. Referring to Figs. 6(a) and (b), in this case length of the coupler link, i.e. l_2 is an variable which need to be calculated. In the finger design, position sensors are embedded in the servo and PIP joint, hence the joint angles θ_1 and θ_3 can be read from the sensors. Using these two joint angles, through simple geometric operation, the real-time length of l_2 can be expressed as

$$l_{2'} = \sqrt{(l_3 \cos\theta_{1''} - l_1 \cos\theta_{3''})^2 + (l_3 \sin\theta_{1''} - l_1 \sin\theta_{3''})^2} \tag{11}$$

where $\theta_{1''}$ and $\theta_{3''}$ stand for the measured angles for θ_1 and θ_3.

Let the original length of the spring be l_{20} such that the deformation of the spring Δl_2 is

$$\Delta l_2 = l_{2'} - l_{20} \tag{12}$$

Then considering the torque exerted on link l_3, referring to Figs. 6(b), there exists the following relation between the input torque $\tau_{1'}$ and the deformation,

$$\tau_{1'} = \tau_{s1} = k_1 \Delta l_2 l_3 \cos\alpha_1 \tag{13}$$

where k_1 is the spring stiffness for springs in the linkages with $k_1 = 4.48$ N/mm, τ_{s1} denotes torque of the servo for driving the linkage, and the angle α_1 as indicated in Figs. 6(a) and (b). By using cosines law, α_1 can be expressed as

$$\alpha_1 = \pi/2 - \arccos\left(\frac{l_{2'}^2 + l_3^2 - \left(l_0^2 + l_1^2 - 2l_0 l_1 \cos\theta_1\right)}{2 l_{2'} l_3}\right)$$

Subsequently, the output torque on the PIP joint $\tau_{3'}$ can be calculated through Eq. (10) as

$$\tau_{3'} = f_2(\tau_{1'}) = \frac{l_3 \sin(\theta_{3''} - \theta_{2''})}{l_1 \sin(\theta_{1''} - \theta_{2''})} \tau_{1'} \tag{14}$$

where angle θ_2'' needs to be calculated through Eq. (2) by using $l_{2'}$ obtained in Eq. (11).

3.3.2. Torque analysis for TST system

MCP-1 joint in the proposed MCR-hand III is driven through the tendon-spring-integrated transmission system. As shown in Fig. 6(a), one end of the tendon, indicated in blue, is connected to a pulley on the output shaft of the motor, diameter of the pulley is denoted as D. The other end of the tendon is fixed on the distal end of a linear spring knotted at point N. MCP joint angle is denoted as θ_{MCP} around joint centre O, which is represented by the rotation angle of OM as shown in Fig. 6(a) and (c). When the finger is in approaching and initial contact stage, the pulley rotates an angle θ_s', and the tendon is pulled from M to M', the spring is not in action (the end of the tendon is located at point N). When the finger is in grasping stage, spring connected to the tendon is in action and deforms (from N to N') when the motor continue to rotates an angle $\Delta\theta_s$. Hence, the motor rotation angle θ_s contains two parts: θ_s' for the case that the spring is not in action, and $\Delta\theta_s$ when the spring is in action, i.e. $\theta_s = \theta_s' + \Delta\theta_s$.

In the case that the spring is not in action, referring to Fig. 6(a) and (c), by using cosines law, length of the tendon l_t can be expressed with respect to the joint angle θ_{MCP} as

$$l_t = \sqrt{a^2 + b^2 - 2ab\cos(\pi - \theta_0 - \theta_{0'} - \theta_{MCP})} \tag{15}$$

where $a = \overline{OM}$ and $b = \overline{OP}$, and angles θ_0 and $\theta_{0'}$ (see Fig. 6(a)) are the initial angles between OM and OP, respectively and the horizontal line passing through point O, when $\theta_{MCP} = 0$ (The tendon is represented by N-M-Q). When the MCP-1 joint is at its initial position with $\theta_{MCP} = 0$, the tendon length is $l_{t0} = \sqrt{a^2 + b^2 - 2ab\cos(\pi - \theta_0 - \theta_{0'})}$.

Assuming that the deformation of the tendon due to external force is negligible, relation between the tendon length and the servo rotation can be formulated as

$$l_{t0} - l_t = D\theta_s' \tag{16}$$

where D is diameter of the pulley mounted on the servo shaft. The toque generated form the elastic wire is not considered in this step.

Further, in the case that the spring is in action in the gasping stage, the MCP-1 joint stops rotating and the servo continues to rotate so as to generate force for object grasping, and the spring deformed. At this stage, rotation angle of the servo is $\Delta\theta_s$, hence deformation of the spring can be derived as

$$\Delta l = D\Delta\theta_s \tag{17}$$

Hence the compression force on the spring and thus tension force on the tendon is

$$F_t = k_2 \Delta l = k_2 D \Delta\theta_s \quad (18)$$

where k_2 is spring stiffness for the spring integrated with the tendon ($k_2 = 9.98$ N/mm in the simulation).

Therefore the actuation torque from the servo is

$$\tau_{s2} = F_t D = k_2 D^2 \Delta\theta_s \quad (19)$$

where $\Delta\theta_s$ can be obtained from the joint sensor in the servo, and the torque generated at the MCP-1 joint is

$$\tau_{MCP1} = F_t a \cos\alpha' - \tau_e = k_2 D \Delta\theta_s a \cos\alpha_2 - \tau_e \quad (20)$$

where, τ_e refers to the torque generated from the elastic wire that $\tau_e = k_0 r \theta_{MCP}$, with $k_0 (k_0 < 0.1k_2)$ being the stiffness of the elastic wire, r being the force arm of the elastic force. Referring to Fig. 6(a), angle α_2 can be deduced by using the sine law as $\alpha_2 = \arccos\left(\frac{b}{l_t}\sin(\pi - \theta_0 - \theta_{0'} - \theta_{MCP})\right)$. It should be noted that in this stage, the friction is not considered.

Further, for the CMC-1 joint in the thumb, since a torsional spring is used to connect the input and output couplings, when the spring is in action joint torque τ_{CMC1} can be derived as

$$\tau_{CMC1} = k_3 (\theta_{s3} - \theta_{CMC1}) \quad (21)$$

where k_3 is spring stiffness of the torsion spring, θ_{s3} is joint angle of the servo for CMC-1 joint, and θ_{CMC1} is the CMC-1 joint angle which can be read from the position sensor embedded in the joint.

Based on the above derivation, torque at each active finger joint can be calculated which leads to the fingertip force analysis in the following section.

3.3.3. Fingertip force analysis and simulation

By using the Jacobian matrix derived in Eq. (8), fingertip wrench for each of the fingers can be formulated as

$$\boldsymbol{F}_{fi} = \left(\mathbf{J}_i^T\right)^{-1} \boldsymbol{\tau}_i \quad (22)$$

where $\boldsymbol{F}_{fi} = (F_{xi}, F_{yi}, F_{zi}, M_{xi}, M_{yi}, M_{zi})$, $\mathbf{J}_i$ is Jacobian for the ith finger obtained in Eq. (8); and $\boldsymbol{\tau}_i = (\tau_{MCP2}, \tau_{MCP1}, \tau_{PIP})$ for the index and middle fingers, $\boldsymbol{\tau}_i = (\tau_{PL}, \tau_{MCP2}, \tau_{MCP1}, \tau_{PIP})$ for the ring and little fingers, and $\boldsymbol{\tau}_i = (\tau_{CMC1}, \tau_{CMC2}, \tau_{MCP})$ for the thumb.

From the torque analysis in Sections 3.3.1 and 3.3.2, and the wrench for the fingertip presented in Eq. (22), given joint angle θ_{sij} (where subscript s stands for servo, i denotes finger number and j joint number in that finger) of the servo that drives an active finger joint, the corresponding finger joint angle θ_{ij} and fingertip force f_{ij} contributed from this joint can be calculated and predicted. This is very useful for controlling the finger for grasping when the fingertip force is obtained from the tactile sensor mounted at the fingertip.

Taking the index finger as an example and for demonstration purpose considering only normal force on pad of the fingertip, given joint angle for the servo at the PIP joint θ_{s24} within its motion range, joint angle for the PIP joint, i.e. θ_{24} and the corresponding normal force f_{n24}, where subscript n stands for normal force, can be computed by using the equations derived above and illustrated in Fig. 8.

From Figs. 8(a) and (b), it can be seen that when θ_{24} is over a specific angle, e.g. 50°, the servo motor cannot deliver maximum torque as it reaches its maximum angle. This phenomenon is more obvious when θ_{24} is over 80° in which the fingertip force is limited to under 2 N. When θ_{24} is below 50°, the fingertip force is limited mainly by the moment arm. The maximum achievable fingertip force occurs at around $\theta_{24} = 50°$, which is approximately 7 N. It is noted that limitations

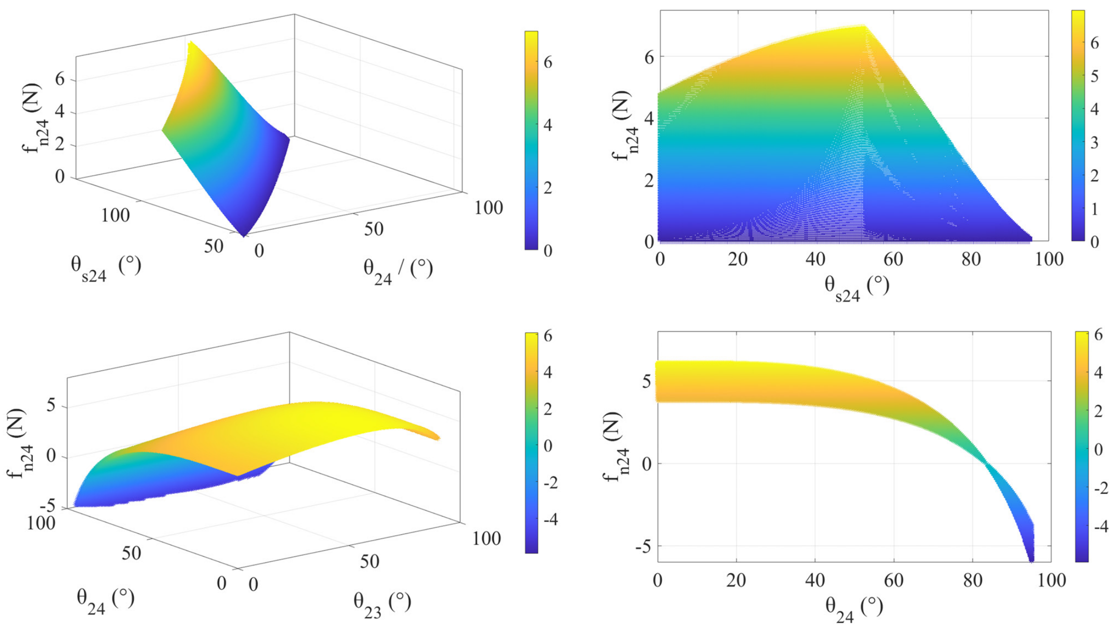

Figure 8: a) Relationship between θ_{s24}, θ_{24} and f_{n24}; b) relation between θ_{24} and f_{n24}; c) relation between θ_{23}, θ_{24} and maximum of f_{n24}; and d) relation between θ_{24} and maximum of f_{n24} when the MCP-1 joint is in action.

from the servos and springs used at the PIP joint in this design are: 1) $\theta_{s24} < 135°$; 2) $\Delta_l < 7$ mm (the maximum elongation of the spring is 7 mm); and 3) $\tau_{servo} < 310$ Nmm (the maximum output toque of motor is 310 Nmm).

Similarly, with the mechanical limitations that $\theta_{s23} < 135°$, $\Delta_l < 5.6$ mm (the maximum elongation of the spring is 5.6 mm), and $\tau_{servo} < 750$ Nmm (the maximum output toque of motor is 750 Nmm), the relationship can be obtained. Figures 8(c) and (d) indicate the normal fingertip force when both the MCP-1 and PIP joints are in action. It can be found that the MCP-1 joint cannot provide normal fingertip force when θ_{24} is over 84°, as the MCP-1 joint rotation causes fingertips to move towards the rear side of the finger. The maximum fingertip force under the action of both the MCP-1 and PIP joints occurs when θ_{24} is relatively small, which is about 6 N.

Through the same computing and simulation approach presented above, the relation between finger joint angle θ_{1j}, servo joint angle θ_{s1j}, and fingertip normal force f_{n1} for the thumb can be also obtained. The results show that in this design the maximum fingertip normal force is around 9.5 N when both the MCP and CMC joints are in action.

From the above derivation, the mappings among the active finger joint θ_{ij}, the actuation servo joint angle θ_{sij} and the corresponding fingertip normal force generated from this referred joint f_{nij} can be obtained such that given any two of them, the other one can be identified. This can be expressed as

$$\begin{cases} \theta_{ij} = g_1\left(f_{nij}, \theta_{sij}\right) \\ f_{nij} = g_2\left(\theta_{ij}, \theta_{sij}\right) \\ \theta_{sij} = g_3\left(\theta_{ij}, f_{nij}\right) \end{cases} \tag{23}$$

From Eq. (23), it can be seen that variables in the LST and TST systems are joint angles, motor rotation angles and joint torques. Structure parameters are the elastic coefficient of the spring which serves as coupler link and lengths of the three links in the four-bar linkage. These three variables are related in three functions such that by given any two of the variables, the third one can be calculated. Hence, knowing the required joint angle and joint torque, we can get the required motor rotation angle. The joint angle is measured by a rotation sensor installed in each finger joint, so the relation for joint torque and motor rotation angle can be confirmed. Eq. (23) can be directly applied in coding to control joint torque. Compared with other solutions, this approach can reduce programming difficulty and the number of sensors.

Hence, from this section kinematics and fingertip forces are characterized and revealed. The results obtained from this section can be verified using experiments based on a physical prototype and can be used for control of the proposed robotic hand.

4. Prototype, Electronics, Sensors and Control

4.1. Prototype, Electronics and Sensors

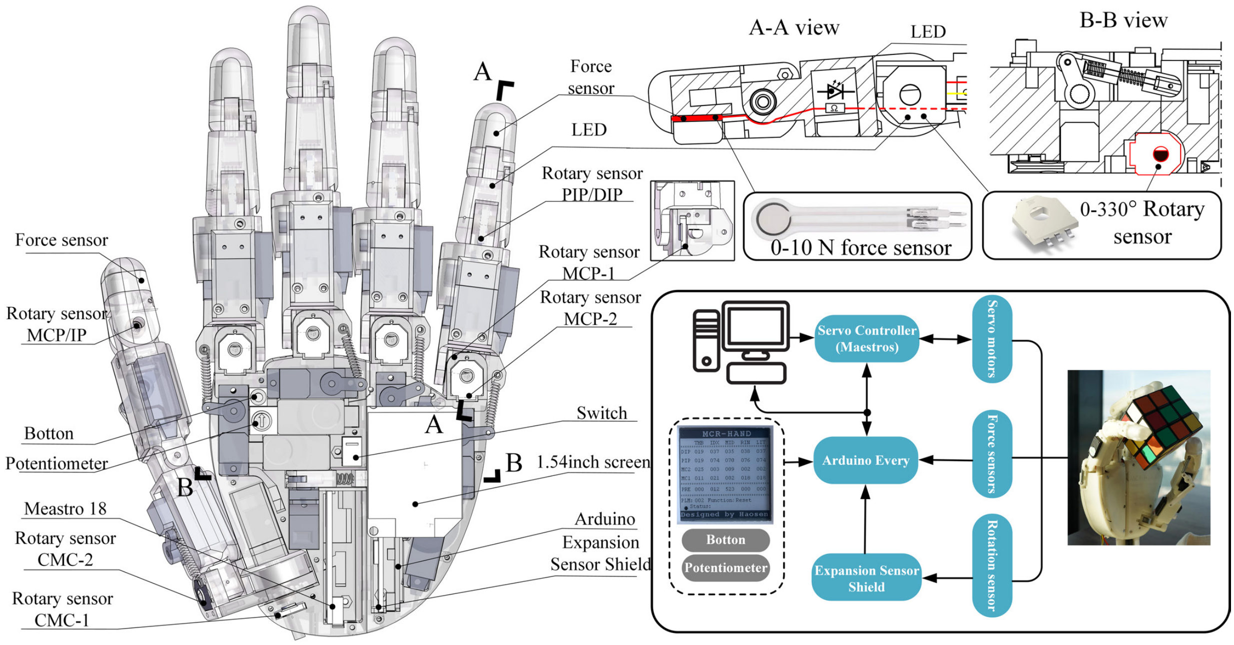

Figure 9: Prototype, electronics, sensing and control of the MCR-Hand III. A total of 5 force sensors and 16 angle sensors are used in MCR-Hand III. The cross-sectional views show the force sensors built inside the fingertips and the rotary sensor built inside the palm, which is used to read the angle of the split palm. The robotic hand can interact with a PC or run programs independently.

Based on the design and analysis presented in the previous sections, physical prototype of the MCR-Hand III was developed as illustrated in Fig. 9. It was mainly fabricated through 3D printing technology. Economical actuators, sensors and controllers are integrated in the hand to keep it affordable for the public. In the prototype, all the driven joints in the MCR-Hand III are equipped with rotary sensors (Bourns 3382G-1-103G, with ±2% linearity) that are connected to a 16-channel sensor shield, which is further connected to the controller (Arduino™ Nano Every). The rotation sensor for the palm joint is shown in the section view (B-B) in Fig. 9. There are 16 servos (3 Bluebird® BMS-207WV servos, 13 MKS® HV6100 servos) and 16 rotary sensors in total. Each fingertip is equipped with a force sensor Interlink Electronics® FSRTM 400 (the standard 400 sensor is a round sensor of 7.62mm in diameter and 0.35mm in thickness) directly connected to the controller. The force sensor applied has ability to measure $0-10$ N normal force, which is selected based on the peak force calculated. As shown in the section view (A-A) in the figure, force sensor is covered with rubber-based tip to increasing friction during object grasping. All the wires are embedded inside the phalanges and palm. 18 springs are used in the prototype: 4 compression springs with a stiffness $k_2 = 9.98$ N/mm and 12.7 mm free length for the MCP-2 joint; 2 compression spring with a stiffness 4.99 N/mm and 6.4 mm free length for the palm joint linkage P/F; 10 extension springs with a stiffness $k_1 = 4.98$ N/mm and 21.6 mm free length; and a torsion spring with a stiffness $k_3 = 47.8$ N/rad.

In order to keep the size of the proposed robotic hand close to the size of an adult human hand, a servo controller Maestros® was used to drive all the servos. This is a controller with eighteen multiple function channels which allow PWM (pulse-width modulation) output and analogue input, its precise and high-resolution servo pulses make the controller well fit high-performance robots. The built-in speed and acceleration controller make it easy to achieve smooth movements. In addition, as aforementioned, Arduino™ Nano Every is chosen to drive the 16-channel expansion sensor shield and 18-channel maestro servo controller.

Further, an intuitive control diagram is proposed, which contains two control schemes. The first scheme is through direct PC control. In this scheme, the servo controller (Maestros) receives digital signals including joint angles, and angular speeds and accelerations from the software interface on the PC and sends PWM signals to the servo motors, leading to the motion of the robotic hand. The current positions of the joints are fed back to the Arduino then to the PC. The second control scheme is identifying the grasping state and the output force automatically, through the sensor reading and the relations between servo, joint angle and fingertip force. The derivation was described in the previous section, and the grasping strategies will be detailed in the following sections.

Moreover, for off-line application a button, a potentiometer and a 1.54-inch screen (with 200 × 200 resolution) form a built-in user interface system in the hand. The screen is programmed to display the joint position and force sensor reading to provide real-time information of the hand.

Cost for the prototype of MCR-Hand III developed in this paper is approximate \$800. Comparing with the commercially available robotic hands listed in Table 3, it can be found that the MCR-Hand III is a low-cost light-weight robotic hand with mechanical compliance, and can provide capabilities for manipulations that require the closest approximation of the human hand.

Table 3: Some commercial robotic hands and the MCR-Hand III

Name	DoF	AN[1]	Weight (kg)	Size[2]	Payload (kg)	FC[3](N)	MC[4]	Price US $
Shadow Hand	24	20	4.3	1.2	4	-	N	> 60,000
Hand-Lite	16	13	2.4	1.2	4	10	N	> 10,000
DLR-HIT Hand II	15	10	1.5	1.0	-	10	N	> 14,000
Schunk Hand	20	9	1.3	1.0	-	5	N	54,000
MCR-Hand III	21	16	< 0.5	1.2	2.5	7	Y	< 800

[1] AN stands for Actuator Number
[2] Here size is the ratio between size of robotic hand and that of an adult human hand.
[3] FC stands for fingertip force
[4] MC stands for Mechanical compliance

4.2. *Fingertip Force Calibration and Validation*

In MCR-Hand III, each fingertip of fingers and thumb is supplied with a force sensor, which is covered with rubber tip and connected to 3.3V DC power through resistance. In order to functionalize the sensor, calibration is carried out with the set-up illustrated in Fig. 10(a). In the calibration process, the sensor is placed on a precision scale, then by applying specified loads on the sensor (which will simultaneously exerted on the scale), and reading the values from both the scale and sensor, the characteristic curve that maps the sensor reading to the corresponding force value can be obtained as shown in Fig. 10(b). From the figure, it can be seen that the curve is approximately composed of two straight lines cornered at a point in which the reading is 90. Hence, from the curve sensor force can be expressed by the sensor reading as

$$f = \begin{cases} 0.01 \times 3.33 \times N_r \ (N), & \text{for } N_r \leqslant 90 \\ 0.01 \times (1.84 \times N_r + 135.2) \ (N), & \text{for } N_r > 90 \end{cases} \tag{24}$$

where N_r stands for the value from reading of the sensor.

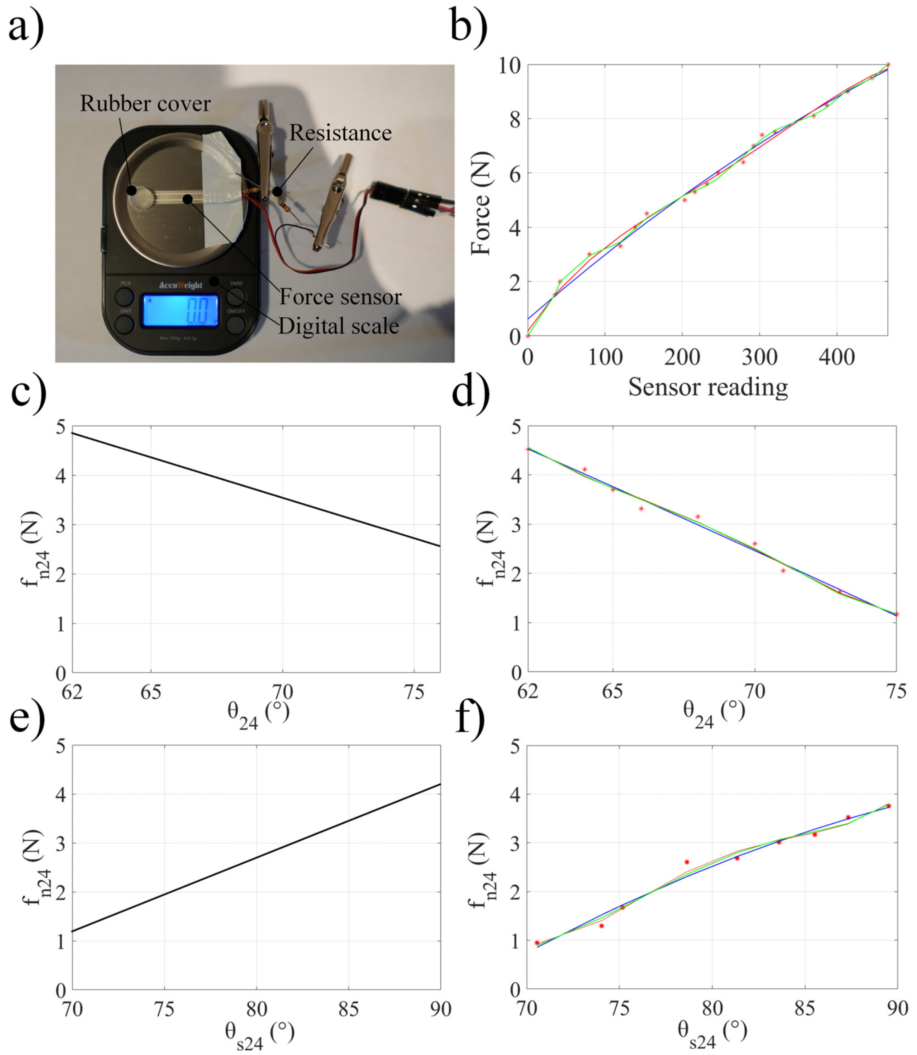

Figure 10: (a) Force sensor calibration set-up; (b) relation between sensor reading and contact force; (c) Theoretical relation between f_{n24} and θ_{24} when θ_{s24} is fixed at 130° of the index finger; (d) Experimental relation between f_{n24} and θ_{24} when θ_{s24} is fixed at 130° of the index finger; (e) Theoretical relation between f_{n24} and θ_{s24} when θ_{24} is fixed at 20° of the index finger; (f) Experimental relation between f_{n24} and θ_{s24} when θ_{24} is fixed at 20° of the index finger.

By using the force sensor attached on the fingertip, the fingertip reading force from the sensor can be compared and verified with the theoretical results obtained with the derivations in the finger force analysis in Section 3.3.

Taking the action of the PIP joint in the index finger as an example, when the servo joint angle θ_{s24} is fixed at 130°, the theoretical relation between the PIP joint angle θ_{24} and the normal force contributed from this joint f_{n24} as obtained with Eq. (23) is illustrated in Fig. 10(c), and the experimental results with the same servo joint angle setting ($\theta_{s24} = 130°$) and different joint angles (ranging from 62° to 75°) is illustrated in Fig. 10(d). Note that, in order to protect the motor and spring, the joint angle has only changed by 13° during the test. It can be found that the experimental curve is very close with the theoretical one, while, the experimental fingertip force is about $0.5N$ less than the theoretical result, it may due to the friction. In addition, Figs. 10(e) and (f) show the theoretical and experimental results relating the fingertip force f_{n24} and the servo joint angle θ_{s24} in the PIP joint. In this case, for the theoretical results, the PIP joint angle θ_{24} is fixed at 20°, and relation between θ_{s24} and f_{n24} is calculated with Eq. (23). For the experimental results, the PIP joint angle θ_{24} is fixed at 20°, the fingertip force is recorded while increasing the motor joint angle θ_{s24} from 70° to 90°. It can be seen that there is still $0.5N$ difference for the fingertip force between the theoretical and experimental results, which indicated that the error source is similar and stable, and thus be compensated. The calibration between the finger joint angles and fingertip forces can then be further used for hybrid position and force control in further study. In addition, through test, we found that the fingertip force of the MCR-Hand III could reach a controllable value of approximately 7N with the servo motor used in the prototype.

4.3. Object Stiffness Identification and Grasping Force Control

In manipulation, stiffness of the targeted objects is an important parameter that must be considered when the robot hand is to grasp an object. There are several ways to determine stiffness of objects, e.g. using external camera with image processing [51], analyzing the force sensor feedback curve from different objects to determine the stiffness [52]. In this section, the process of identifying object stiffness using the compliant transmission systems from MCR-Hand III is presented, together with different strategies for object grasping.

The process for identifying object stiffness and grasping is summarised in the flowchart as shown in Fig. 11, it consists of three stages, i.e. the approaching and contacting stage, measuring stage, and grasping stage.

4.3.1. Approaching and Contacting Stage

In the approaching and contacting stage, the robotic finger and thumb will flex to the targeted object from fully extended until the contacting is detected. There are two schemes for the MCR-Hand III to identify object contact as follows.

The first, by using force feedback at the fingertips. For PIP/DIP, MCP-1 joint in the fingers, and IP and CMC-1 joints in the thumb, flexion of these joints may cause an increase in the fingertip normal force. Hence force sensors at the fingertips are used to detect contact based on the sensor reading, which may reaches a value above specified threshold ($f > f_{threshold}$). Once the system detects contact force (e.g. f^1_{nij}) from sensor reading, which can be considered as the finger has touched the object, the corresponding motor stops rotating.

The second, for the joints which force feedback at the fingertips can not be used, e.g. the CMC-2 joint, flexion of these joints causes no change in fingertip normal force. In this case the contact identification process relies on the relationship between servo joint angle θ_{sij} and joint angle θ_{ij} when the normal fingertip force $f_{nij} = 0$. At the stage if fingers and thumb flex, joint angles θ_{sij} and θ_{ij} are compared real-time. When there is no contact force applied, i.e. $f_{nij} = 0$, θ_{sij} and θ_{ij} has the following relationship according to Eq. (23),

$$\theta_{ij} = g_1\left(f_{nij} = 0, \theta_{sij}\right) \tag{25}$$

After the fingers and thumb touch the object, the motors continue to rotate. This leads to the deformation of springs in the LST and TST systems such that θ_{ij} and θ_{sij} no longer have the relation in Eq. (25), θ_{ij} is smaller than the one obtained from Eq. (25) as

$$\theta_{ij} < e \cdot g_1\left(f_{nij} = 0, \theta_{sij}\right) \tag{26}$$

Here, a sensitivity coefficient e satisfying $0 < e < 1$ is introduced to avoid misjudgement. Once all the fingers and thumb are in contact with the object, further motion of the finger and thumb is forbidden, and the hand enters measuring stage. If the joint angles reach their maximum, the servos stop and the process ends.

4.3.2. Measuring stage

The measuring stage aims at estimating stiffness of the object grasped by the hand. After the fingers contact the object, further motion of the servos lead to deformation of the springs, resulting in the increase of contact force, deformation of the object follows subsequently if the objects is deformable.

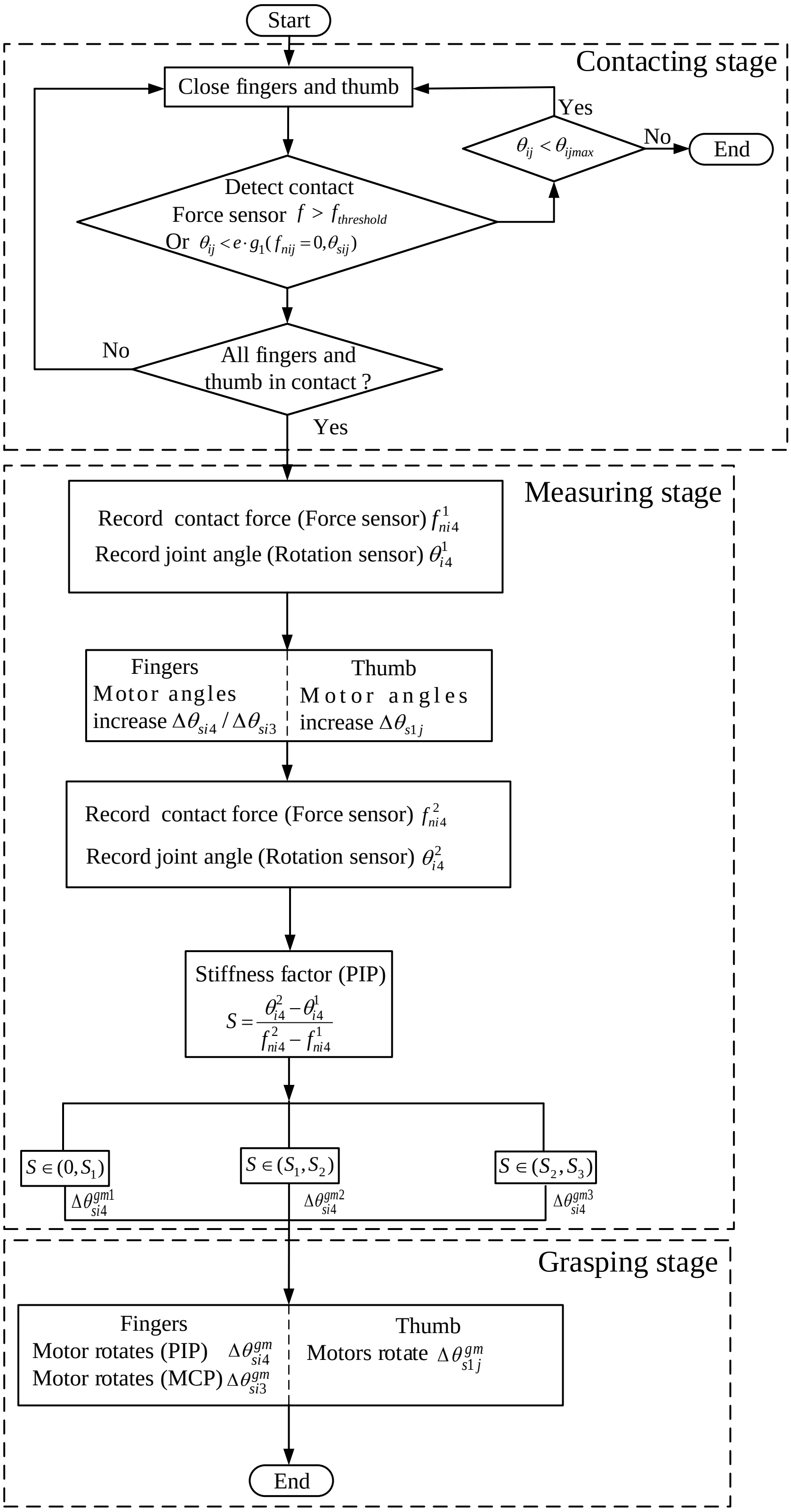

Figure 11: Flowchart for grasping based on object stiffness. The process is divided into three stages, i.e. contacting, measuring and grasping stage. In the contacting stage, the robotic finger touches the object's surface and the contact is detected. In the measuring stage, the robotic hand will apply a certain force, to calculates the stiffness factor S of the object, and evaluate its softness. In the grasping stage, different grasping forces are applied according to different stiffness factors.

The amount of deformation of the target object is positively related to the finger joint angle θ_{ij} and substantially change of the associated servo joint angle $\Delta\theta_{sij}$ (e.g., if the target object is deformable, after the fingers and thumb contact the object, as the motor continues rotating an angle $\Delta\theta_{sij}$, the fingertip force increases and the target object deforms due to the force, simultaneously in the process joint angles of the fingers and thumb increase). For objects with different stiffness, the deformation is different, and so are increases of joint angles. Therefore, deformation of the objects can be quantified by the joint angle difference under the same $\Delta\theta_{sij}$ (Note that here we consider that the size of different objects are similar. Otherwise, the deformation should be positively related to the distance change of the fingertip). To distinguish the different stiffness, a stiffness factor S is introduced. This factor is expressed as the ratio between the joint angle difference $\Delta\theta_{ij}$ and the fingertip force difference Δf_{nij} when the servo continues to rotate an angle $\Delta\theta_{sij}$ after contacting,

$$S = \frac{\Delta\theta_{ij}}{\Delta f_{nij}} = \frac{\theta_{ij}^2 - \theta_{ij}^1}{f_{nij}^2 - f_{nij}^1} \tag{27}$$

where θ_{ij}^1 and θ_{ij}^2 are the joint angles before and after the motor continues to rotate by angle $\Delta\theta_{sij}$, and f_{nij}^1 and f_{nij}^2 are the fingertip force before and after the same rotation of the motor.

Deformation of the grasped object is proportional to factor S. It is understandable that under the same fingertip force, if the object is formed of soft material, factor S is greater, and on the contrast, S is smaller if the object is made of rigid material.

In addition, before the measuring process the servo joint angle $\Delta\theta_{sij}$ for each finger joint needs to be specified so that the fingers perform further grasping for measuring the stiffness of the targeted object. After the approaching and contacting stage, the MCP-1 and PIP/DIP joints are held at the same time so as to provide grasping force at fingertip. During the measurement of object stiffness factor, fingertip forces generated by the MCP-1 joint and the PIP/DIP joint maintain equal; in the meanwhile, the resultant force generated by multiple fingers and force from the thumb are equal.

To start with, we define an abbreviation MCRA for the angle that motor/servo continues to rotate after the contact stage, i.e. $\Delta\theta_{sij}$. Further, superscript 1 stands for the angle before measuring, and superscript 2 for the joint angle after measuring. Then, object stiffness factor S can be identified and estimated through the following steps.

Step 1: For the fingers, through a series of tests and experiments according to objects to be grasped, we first set and specify MCRA of the PIP joint as $\Delta\theta_{si4}$, then MCRA for the MCP-1 joint $\Delta\theta_{si3}$ in the same finger is calculated in terms of $\Delta\theta_{si4}$ as follows.

In the PIP joint, let the driving servo joint angle be θ_{si4}^1 when the finger contacts with object, after the motor continues to rotate by $\Delta\theta_{si4}$, the new motor joint angle θ_{si4}^2 is

$$\theta_{si4}^2 = \theta_{si4}^1 + \Delta\theta_{si4} \tag{28}$$

With θ_{si4}^2, the normal fingertip force from the PIP/DIP joint after the measuring, i.e. f_{ni4}^2 can be estimated by using Eq. (23) as

$$f_{ni4}^2 = g_2\left(\theta_{i4}^1, \theta_{si4}^2\right) \tag{29}$$

Note that herein the joint angle at contacting stage θ_{i4}^1 is used to estimate the fingertip force because the joint angle after the measuring stage θ_{i4}^2 is unknown.

As aforementioned, fingertip normal force generated from the PIP joint f_{ni4}^2 and MCP-1 joint f_{ni3}^2 after measuring are equal such that it has $f_{ni3}^2 = f_{ni4}^2$. With f_{ni3}^2, using Eq. (23) the MCRA for the MCP-1 joint, $\Delta\theta_{si3}$ can be calculated as follows:

$$\theta_{si3}^2 = g_3\left(\theta_{i3}^1, f_{ni3}^2\right) \tag{30}$$

and hence

$$\Delta\theta_{si3} = \theta_{si3}^2 - \theta_{si3}^1 \tag{31}$$

Where θ_{i3}^{1} is the MCP-1 joint angle at contacting stage.

In the above calculations, angles θ_{i4}^{1} and θ_{i3}^{1} at the contacting stage are read from sensors. The motors driving the MCP-1 and PIP joints rotate simultaneously, and fingers involved in the grasping performance share the same $\Delta\theta_{si4}$ and $\Delta\theta_{si3}$.

Step 2: For the thumb, the MCRA $\Delta\theta_{s1j}$ is calculated in terms of that of the fingers $\Delta\theta_{si4}$ as the force provided by the thumb f_{n1j}^{2} is opposite and equal to the resultant force generated by all the fingers involved. That is

$$f_{n1j}^{2} = \sum_{1}^{N} f_{ni4}^{2} \tag{32}$$

Where f_{n1j}^{2} and f_{ni4}^{2} refer to the fingertip force of thumb and a single finger, respectively. N refers to the number of fingers involved.

Then, MCRA for the thumb $\Delta\theta_{s1j}$ can be calculated by using Eq. (23) as

$$\theta_{s1j}^{2} = g_3\left(\theta_{1j}^{1}, f_{n1j}^{2}\right) \tag{33}$$

and thus

$$\Delta\theta_{s1j} = \theta_{s1j}^{2} - \theta_{s1j}^{1} \tag{34}$$

Where θ_{1j}^{1} is the joint angle at contacting stage, and θ_{s1j}^{1} is the motor joint angle for the thumb at contacting stage.

Subsequently, using Eq. (34) the MCRA at each joint in the thumb $\Delta\theta_{sij}$ can be determined. The motors involved in the grasping hence rotate the corresponding angle $\Delta\theta_{sij}$ to generate the contact forces for the test object. The targeted object then deforms due to the contact forces, and the joint angles of the fingers and thumb increase due to the deformation. Changes of the joint angles can be read directly from the rotation sensors, which leads to the calculation of stiffness factor of the object through Eq. (27).

Step 3: In order to obtain S in Eq. (27), the next step is to calculate the change of fingertip normal force Δf_{nij}.

For the joints that can use force feedback from fingertip, such as the PIP/DIP, MCP-1 joints in the fingers, and the IP, CMC-1 joints in the thumb, flexion of these joints cause increases in fingertip normal force. Hence, the reading from fingertip force sensor before and after the measuring stage can be directly used to calculate the fingertip force increase. On the other hand, for the joints that cannot use force feedback, such as the CMC-2 joint in the thumb, fingertip normal force change caused by this joint needs to be calculated by using Eq. (23). The fingertip force from this joint before and after the measuring stage are

$$f_{nij}^{1} = g_2\left(\theta_{ij}^{1}, \theta_{sij}^{1}\right) \text{ and } f_{nij}^{2} = g_2\left(\theta_{ij}^{2}, \theta_{sij}^{2}\right) \tag{35}$$

and hence from the above the fingertip force difference can be obtained as

$$\Delta f_{nij} = f_{nij}^{2} - f_{nij}^{1} \tag{36}$$

where θ_{ij}^{1} and θ_{ij}^{2} are the joint angles before and after measuring stage, which can be read from the joint sensors. θ_{sij}^{1} and θ_{sij}^{2} are motor joint angles before and after measuring which are known from the previous step.

Step 4: Based on the above derivation, stiffness factor of the object can be calculated using Eq. (27). For example, if we use PIP joint in the index finger to calculate the stiffness factor of the object, it has:

$$S = \frac{\theta_{24}^{2} - \theta_{24}^{1}}{f_{n24}^{2} - f_{n24}^{1}} \tag{37}$$

In the daily life manipulation, objects are of various stiffness. In this study, based on a series of grasping tests (the stiffness factors for different objects were measured using Eq. (37), i.e. a cake, a cup, etc.), they are roughly divided into three categories according to their stiffness from rigid to soft. Object with $S \leq 1$ is defined as rigid; with $1 < S \leq 5$ is semi-soft; and with $S > 5$ is soft. In this stage, we assume that the object's stiffness is uniform.

4.3.3. *Grasping stage*

After the measuring stage which identifies stiffness of the targeted object, it is grasping stage. In this stage, in order to grasp the object, servos in the fingers which are involved in the grasp need to rotate further. Similar to the previous section, in order to find the rotation angels for each servo in the fingers and thumb, the further angle change in the PIP joint in a finger needs to be identified and specified. Herein, the further motor rotation at the PIP joint of a finger is denoted as $\Delta\theta_{si4}^{\lambda r}$, with λ stands for grasping stage and r = 1, 2 and 3 for the cases that the object is rigid, semi-soft and soft, respectively. For objects of different stiffness, the value $\Delta\theta_{si4}^{\lambda r}$ are different. Based on a series of tests, the approximate values of $\Delta\theta_{si4}^{\lambda r}$ for different objects are $\Delta\theta_{si4}^{\lambda 1} = 10°$, $\Delta\theta_{si4}^{\lambda 2} = 6°$, and $\Delta\theta_{si4}^{\lambda 3} = 4°$. Using the specified angle $\Delta\theta_{si4}^{\lambda r}$, further servo rotation angle at joints in the fingers and thumb involved in the grasping can be calculated based on the same equations derived in the measuring stage.

4.3.4. *Autonomous grasping tests*

In this section, in order to demonstrate the use of sensory systems and the real-time object stiffness identification and control approach presented above, autonomous grasping tests are conducted. The index, middle fingers and the thumb are involved in this test. Motions from PIP/DIP and MCP joints (which are associated with fingertip force feedback) in the finger are mainly considered, while CMC-2 joint (without force feedback) in thumb is used to assist completing the grasping. Further, to identify contact, the threshold for force sensor is set to 20, with the sensitivity coefficient $e = 0.9$, and the measuring time is set as 2 s (to calculate the average value during the measuring time). To simplify the algorithm, only the rotation sensor and force sensor in the index finger is used to calculate the stiffness factor.

Three different objects with three stiffness factors, i.e. a cake (see Fig. 12(a)), a plastic cup (see Fig. 12(b)) and a glass cup (see Fig. 12(c)), are used for the autonomous grasping tests, sizes of the cups are similar. In all the tests, once the grasping stage is accomplished, the MCR-Hand III is raised by a 1-DOF customised supporting arm.

Throughout the tests, fingertip forces and joint angles for the PIP, MCP, and CMC-2 joints are recorded. Each test was repeated for 10 times. For the soft and medium stiffness objects, every test was successful and the targeted objects were lifted by the arm successfully without damage (could return to its original shape after grasping). However, 3 out of 10 tests failed for the rigid object, the targeted object slipped out of the hand during the tests. This occurs because for objects with high stiffness, due to the smaller deformation, the contact area is small, and thus contact with the robotic hand is close to point contact. When only the tips of the finger and thumb are in contact with the objects, it cannot provide a stable force to keep the targeted object in balance while lifting, and thus the object deflects and slips off. For all the tests, joint angles and fingertip forces for the approaching and contacting stage, measuring stage and grasping stage, are shown in Fig. 12. It can be found from the figure that, stiffness factor detected for the cupcake is $S = 9.65$ and the grasping force used is 1.9 N; stiffness factor measured for the plastic cup is $S = 2.62$ and the grasping force is 3.8 N; and stiffness factor for the glass cup is $S = 0.465$ with grasping force 5.9 N.

Through these tests, it demonstrates that the LST, TST systems proposed in this paper are efficient and feasible for detecting contact and for measuring stiffness of the targeted object without introducing extra sensors. However, avoiding slippage in rigid object grasping is issue to be considered for future design.

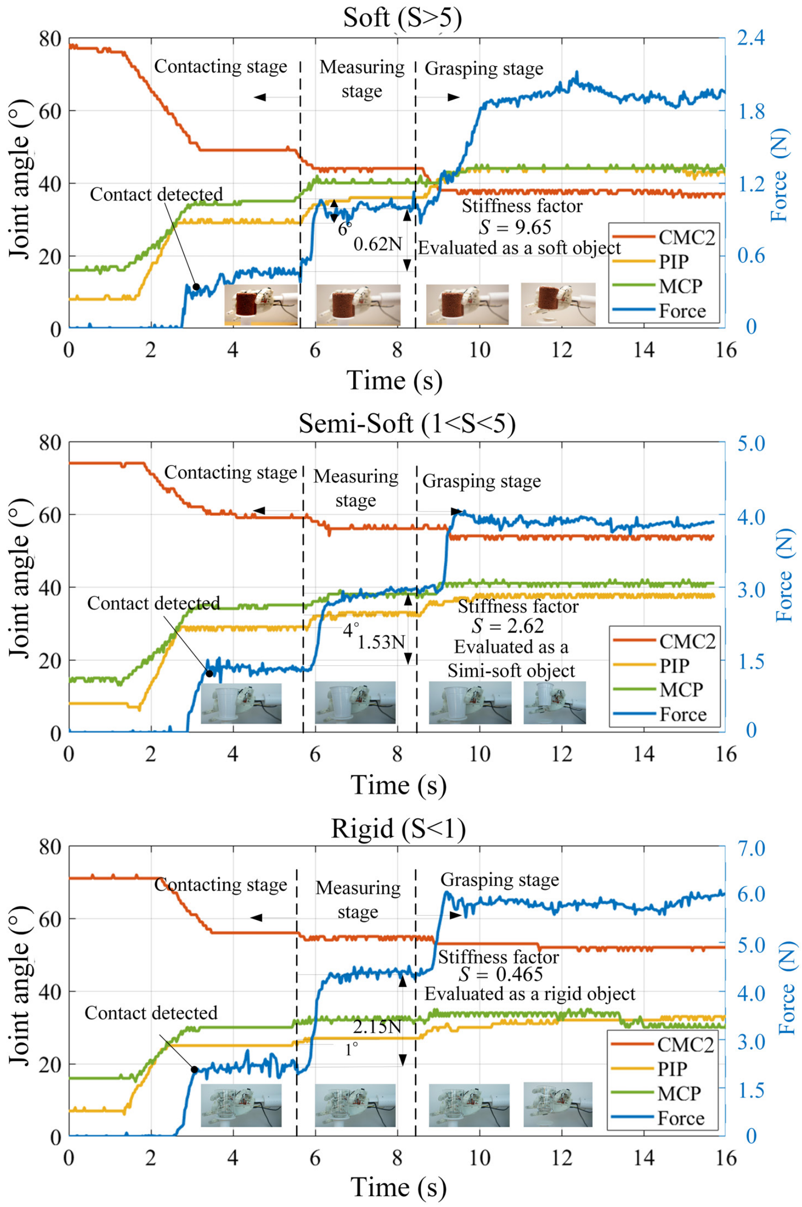

Figure 12: Joint angle and fingertip force during autonomous grasping tests. Through the measuring stage, the stiffness factors S of the three objects are 9.65, 2.62, 0.465, respectively, which are evaluated as soft (a), Semi-soft (b), and rigid (c). Therefore, three different gripping forces are applied to the grasping stage.

5. Empirical Study and Evaluation

5.1. Grasping Evaluation Based on Cutkosky Taxonomy

One of the main functions of robotic hands is to assist human for work in factories and the other civilian daily life operations, hence in this section the Cutkosky Taxonomy [53] is used to evaluate the performance of the proposed robotic hand. There are 16 different types of grasping poses in the Cutkosky taxonomy, which are divided into power grasping and precision grasping. By using the MCR-Hand III, a static evaluation was conducted by determining whether the hand can complete the grasping poses listed in the Cutkosky taxonomy, and the experimental results are presented in Fig. 13. From Fig. 13, it can be seen that the MCR-Hand is capable of implementing both power and precision grasp including heavy wrap, thumb-index finger grip, spherical power

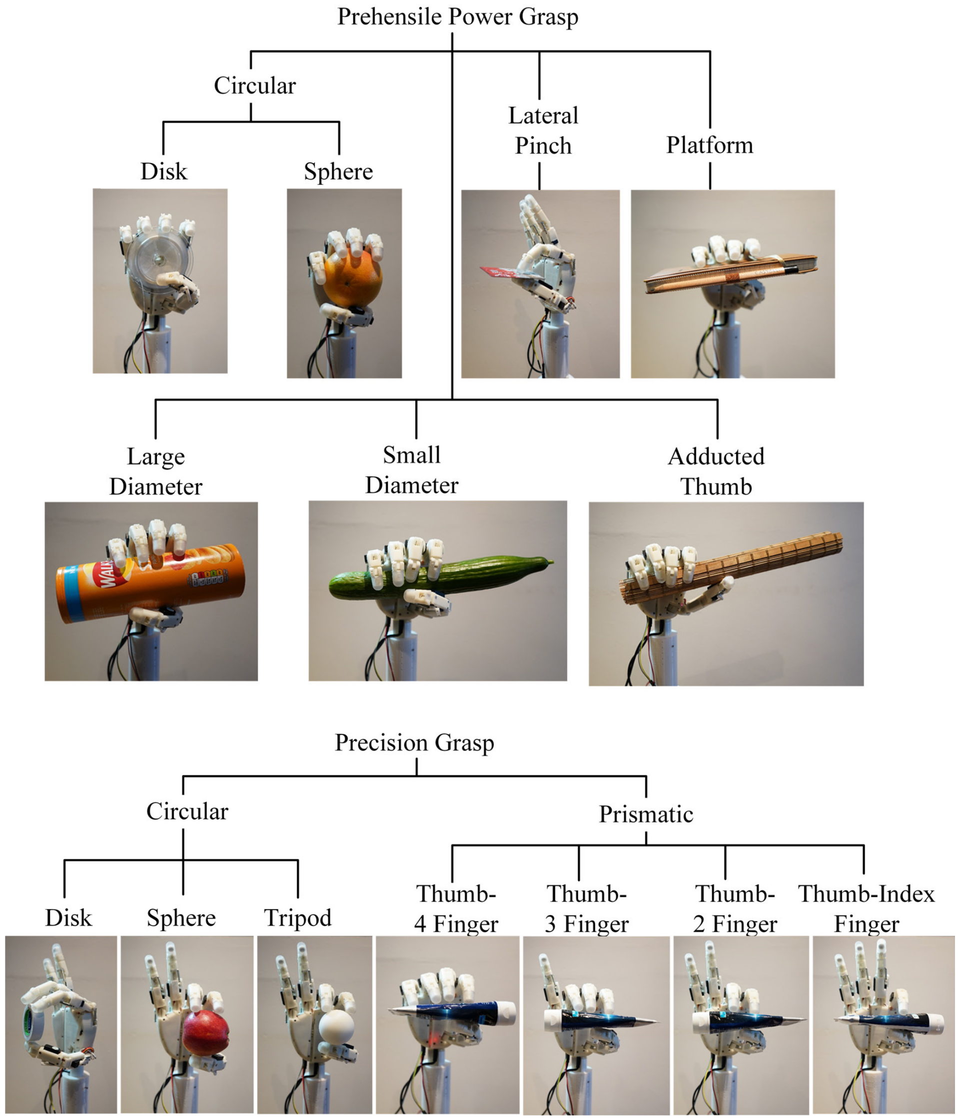

Figure 13: Grasping performance of the MCR-Hand III according to Cutkosky taxonomy.

grasp, medium wrap, and lateral pinch grip. The more grasping and manipulation studies can be conducted further for various applications.

5.2. Grasping with Deformable Object

In this section, the robotic hand will be tested to grasp a thin plastic cup filled with 80% of its volume by water of about 150 g, the grasps will be conducted by using different combination of fingertip forces. The purposed of this test is to check whether the hand is capable of automatically generating adaptable force that is suitable for grasping medium soft objects.

The setting-up of this test is shown in Fig. 14(a), the robotic hand is attached to a 1-DOF robotic arm. The plastic cup is placed on a platform, locations of the platform and cup are fixed to the same position throughout the test. In this test, only the index and middle fingers, and the thumb participate. The PIP and MCP-1 joints of the fingers, and the CMC-2 joint of the thumb are actuated to generate sufficient fingertip forces.

In the test, finger joint and servo angles were recorded (with sensors at the joints) when the finger touched the cup surface. Then we increased angles of the servos (by 3° for the PIP joint, 2° for the MCP joint, and 4° for the CMC-2 joint) to increase the contact forces between the fingertips and cup. Following this, the robotic arm lifted the robotic hand. Readings from servo angle, force sensor, grasp state, deformed situation of plastic cup were all recorded. The test was repeated until the cup was totally deformed.

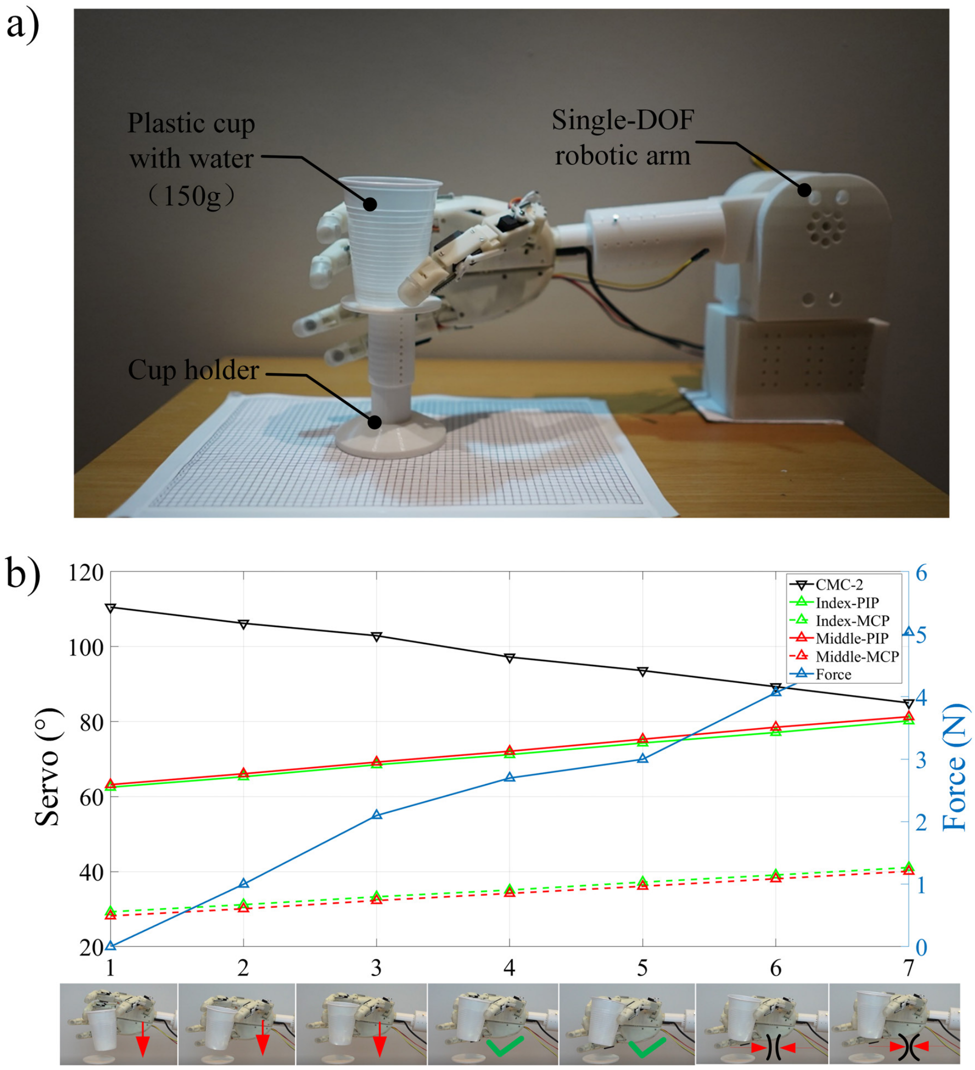

Figure 14: Grasping performance with force control. (a) Experiment set-up for test of lifting a cup; (b) Experiment results for cup lifting test.

The test was repeated seven times, and the results are shown in Fig. 14(b). The first test was carried out at the initial servo angles when fingertips touched the cup surface, results show the slippage occurred during the lifting process (indicated in downward arrow in Fig. 14(b)) and hence the first experiment was considered failure. Servo angles in the second and third tests were increased, where the increment of servo angles in the finger joints are shown in Fig. 14(b). In these two tests, the cup was still not firmly held during lift, and thus they were considered failed. Then, with the joint angles in the fingers continued to increases, tests indicated that the cup could be held firmly with no deformation when the servo angles reached the specified values, as shown in the fourth and fifth tests in Fig. 14 (b). Further increasing the servo angles, as the sixth and seventh tests in Fig. 14(b), lead to severe deformation of the cup such that the cup could not return to its original shape after the grasping, thus these two tests were also considered failed.

These tests indicate that it is important to have the grasping force controlled while handling soft material-based objects, like cakes, flowers and jelly. The proposed robotic hand can fulfil such an operation.

5.3. Further Dexterous Manipulation Test

Other than grasping objects, robotic hands are required to complete manipulation tasks for the highly demands in industry and domestic use. There is no single standard to distinguish the manipulability of a robotic hand especially for dexterity ones. In order to demonstrate manipulability of the MCR-Hand III, the hand was attached to a fixed arm (with no DOF involved) and placed on an electronic piano as illustrated in Fig. 15, then with pre-programmed sequences, the proposed robotic hand successfully played a short section of a piece. The performance was implemented and recorded as shown in the video attached.

Figure 15: The MCR-Hand III in piano manipulation.

6. Conclusions

In this paper, a low-cost anthropomorphic robotic hand, MCR-Hand III, was for the first time presented. This novel robotic hand has a hybrid transmission system that combines both tendon-driven and linkage-driven systems, which leads to the design of a robotic hand that is close to the size of an adult human hand and can imitate all DOFs of a human hand. Mechanical compliance was also introduced by integrating mechanical springs with the linkage- and tendon-driven systems. Such compliance not only secures the robotic hand from unexpected external disturbance and force, but also provides the hand with functions of contact detection, object stiffness identification, and better grasping and manipulation performance. Kinematics and force analysis of the proposed robotic hand were presented supported by numerical simulation results, laying background for comparison and evaluating the features of the proposed hand. By using 3D printing technology, prototype of the proposed hand was developed integrated with economic sensory and control systems, leading to an affordable full functional robotic hand. Using the prototype, calibration and validation of the sensory systems were accomplished, and an object stiffness identification and grasping force control algorithm was developed, tested and evaluated. Then, based on the Cutkosky taxonomy, grasping and manipulation performance of the MCR-Hand III was verified, with extended experiments in deformable object grasping and piano piece playing.

The proposed robotic hand can generate up to 7 N controllable fingertip force. The overall weight of the hand is only about 490 g. The hand is in the size that is similar to a male adult hand, and the prototype hand costs less than $800 which makes it affordable for the wider public in various applications.

This paper hence has presented an affordable full-functional lightweight robotic hand which is suitable for lightweight robotic system integration with applications in the fields such as fruit and food processing, human-robot interaction, and autonomous product assembly.

Acknowledgements

This work is partly supported by the projects of National Natural Science Foundation of China under Grant No. 91948302 and No. 91848204, and the project of National Key R&D Program of China under No. 2018YFC2001300.

References

[1] R. Tomovic, G. Boni, An adaptive artificial hand, IRE Transactions on Automatic Control 7 (3) (1962) 3–10.

[2] C. Piazza, G. Grioli, M. G. Catalano, A. Bicchi, A century of robotic hands, Annual Review of Control, Robotics, and Autonomous Systems 2 (1) (2019) 1–32.

[3] K. Tai, A. R. EI-Sayed, M. Shahriari, M. Biglarbegian, S. Mahmud, State of the art robotic grippers and applications, Robotics 5 (2) (2016) 11.

[4] D. S. Childress, Historical aspects of powered limb prosthese, Clinical Proesthetics & Orthotics 9 (1) (1985) 2–13.

[5] T. Okada, Computer control of multjointed finger system for precise object-handing, IEEE Transactions oon Systems, Man and Cybernetics 12 (3) (1982) 289–299.

[6] S. Jacobsen, E. Iversen, D. Knutti, R. Johnson, K. Biggers, Design of the Utah/M.I.T. dextrous hand, in: 1986 IEEE International Conference on Robotics and Automation, Vol. 3, New York, USA, 1986, pp. 1520–1532.

[7] Y. Nakano, M. Fujie, Y. Hosada, Hitachi's robot hand, Robotics Age 6 (7) (1984) 18–20.

[8] A. Caffaz, G. Cannata, The design and development of the DIST-hand dextrous gripper, in: 1998 IEEE International Conference On Robotics And Automation, Leuven, Belgium, 1998, pp. 2075–2080.

[9] H. Liu, J. Butterfass, S. Knoch, P. Meusel, G. Hirzinger, A new control strategy for DLR's multisensory articulated hand, IEEE Control Systems Magazine 19 (2) (1999) 47–54.

[10] J. Butterfass, M. Grebenstein, H. Liu, G. Hirzinger, DLR-hand II: Next generation of a dextrous robot hand, in: Proceedings of the 2001 IEEE International Conference on Robotics & Automation, Seoul, Korea, 2001.

[11] C. S. Lovchik, M. A. Diftler, The Robonaut hand: a dexterous robot hand for space, in: Proceedings 1999 IEEE International Conference on Robotics and Automation, Vol. 2, 1999.

[12] L. B. Bridgwater, C. A. Ihrke, M. A. Diftler, M. E. Abdallah, N. A. Radford, J. M. Rogers, S. Yayathi, R. S. Askew, D. M. Linn, The Robonaut 2 hand - designed to do work with tools, in: 2012 IEEE International Conference on Robotics and Automation, Minnesota, USA, 2012, pp. 3425–3430.

[13] J. S. Dai, D. L. Wang, L. Cui, Orientation and workspace analysis of the multifingered metamorphic hand - Metahand, IEEE Transactions on Robotics 25 (4) (2009) 942–947.

[14] G. Wei, J. S. Dai, S. Wang, H. Luo, Kinematic analysis and prototype of a metamorphic anthropomorphic hand with a reconfigurable palm, International Journal of Humanoid Robotics 8 (3) (2011) 459–479.

[15] Z. Gao, G. Wei, J. S. Dai, Inverse kinematics and workspace analysis of the metamorphic hand, Journal of Mechanical Engineering Science, Proc. IMechE, Part C. 229 (5) (2015) 965–975.

[16] T. Laliberte, L. Birglen, C. M. Gosselin, Underactuation in robotic grasping hands, Machine Intelligence & Robotic Control 4 (3) (2002) 1–11.

[17] M. Catalano, G. Grioli, E. Farnioli, A. Serio, C. Piazza, A. Bicchi, Adaptive synergies for the design and control of the pisa/iit softhand, The International Journal of Robotics Research 33 (5) (2014) 768–782.

[18] R. Deimel, O. Brock, A novel type of compliant and underactuated robotic hand for dexterous grasping, International Journal of Robotics Research 35 (2016) 161–185.

[19] S. Terryn, J. Brancart, D. Lefeber, G. Van Assche, B. Vanderborght, Self-healing soft pneumatic robots, Science Robotics 2 (2017) eaan4268.

[20] J. Nassour, V. Ghadiya, V. Hugel, F. Hamker, Design of new sensory soft hand: combining airpump actuation with superimposed curvature and pressure sensors, in: 2018 IEEE International Conference on Soft Robotics (RoboSoft), 2018, pp. 164–169.

[21] J. K. Salisbury, J. J. Craig, Articulated hands: force control and kinematic issue, International Journal of Robotics Research 1 (1) (1982) 4–17.

[22] A. D. Deshpande, Z. Xu, M. J. V. Weghe, B. H. Brown, J. Ko, L. Y. Chang, D. D. Wilkinson, S. M. Bidic, Y. Matsuoka, Mechanisms of the anatomically correct testbed hand, IEEE/ASME Transactions on Mechatronics 18 (1) (2013) 238–250.

[23] G. Palli, C. Melchiorri, G. Vassura, U. Scarcia, L. Moriello, G. Berselli, A. Cavallo, G. D. Maria, C. Natale, S. Pirozzi, C. May, F. Ficuciello, B. Siciliano, The DEXMART hand: Mechatronic design and experimental evaluation of synergy-based control for human-like grasping, The International Journal of Robotics Research 33 (5) (2014) 799–824.

[24] T. Mouri, H. Kawasaki, K. Yoshikawa, J. Takai, S. Ito, Anthropomorphic robot hand: Gifu hand III, in: International Conference on control, Automation and Systems, 2002, pp. 1288–1293.

[25] J. Ueda, Y. Ishida, M. Kondo, T. Ogasawara, Development of the NAIST-hand with vision-based tactile fingertip sensor, in: Proceedings of the 2005 IEEE International Conference on Robotics and Automation, Barcelona, Spain, 2005, pp. 2332–2337.

[26] M. L. Kontoudis, George P., K. G. Vamvoudakis., An adaptive, humanlike robot hand with selective interdigitation: Towards robust grasping and dexterous, in-hand manipulation, in: IEEE-RAS 19th International Conference on Humanoid Robots (Humanoids), 2019, pp. 251–258.

[27] C. D. Santina, C. Piazza, G. Grioli, M. G. Catalano, A. Bicchi, Toward dexterous manipulation with augmented adaptive synergies: The Pisa/IIT softhand 2, IEEE Transactions on Robotics 34 (5) (2018) 1141–1156.

[28] P.-H. Kuo, A. D. Deshpande, Muscle-tendon units provide limited contributions to the passive stiffness of the index finger metacarpophalangeal joint, Journal of Biomechanics 45 (15) (2012) 2531–2538.

[29] G. A. Pratt, M. M. Williamson, Series elastic actuators, in: Proceedings 1995 IEEE/RSJ International Conference on Intelligent Robots and Systems. Human Robot Interaction and Cooperative Robots, 1995, pp. 399–406.

[30] G. Tonietti, R. Schiavi, A. Bicchi, Design and control of a variable stiffness actuator for safe and fast physical human/robot interaction, in: Proceedings of the 2005 IEEE International Conference on Robotics and Automation, Barcelona, Spain, 2005, pp. 526–531.

[31] K. Kong, J. Bae, M. Tomizuka, A compact rotary series elastic actuator for human assistive systems, IEEE/ASME Transactions on Mechatronics 17 (2) (2012) 288–297.

[32] P.-H. Kuo, A. D. Deshpande, Novel design of a passive variable stiffness joint mechanism: Inspiration from biomechanics of hand joints, in: Proceedings of the ASME 2013 Dynamic Systems and Control Conference, Vol. 2, 2013, p. V002T28A003.

[33] L. U. Odhner, L. P. Jentoft, M. R. Claffee, N. Corson, Y. Tenzer, R. R. Ma, M. Buehler, R. Kohout, R. D. Howe, A. M. Dollar, A compliant, underactuated hand for robust manipulation, The International Journal of Robotics Research 33 (5) (2014) 736–752.

[34] C. Ott, A. Albu-Schaffer, A. Kugi, G. Hirzinger, On the passivity-based impedance control of flexible joint robots, IEEE Transactions on Robotics 24 (2) (2008) 416 – 429.

[35] T. D. Niehues, P. Rao, A. D. Deshpande, Compliance in parallel to actuators for improving stability of robotic hands during grasping and manipulation, The International Journal of Robotics Research 34 (3) (2015) 256–269.

[36] M. C. Carrozza, G. Cappiello, G. Stellin, F. Zaccone, F. Vecchi, S. Micera, P. Dario, A cosmetic prosthetic hand with tendon driven under-actuated mechanism and compliant joints: Ongoing research and preliminary results, in: Proceedings of the 2005 IEEE International Conference on Robotics and Automation, Barcelona, Spain, 2005, pp. 2661–2666.

[37] M. Controzzi, F. Clemente, D. Barone, A. Ghionzoli, C. Cipriani, The SSSA-MyHand: A dexterous lightweight myoelectric hand prosthesis, IEEE Transactions on Neural Systems and Rehabilitation Engineering 25 (5) (2017) 459–468.

[38] R. B. N. Scharff, E. L. Doubrovski, W. A. Poelman, P. P. Jonker, C. C. L. Wang, J. M. P. Geraedts, Towards behavior design of a 3D-printed soft robotic hand, in: C. Laschi, J. Rossiter, F. Iida, M. Cianchetti, L. Margheri (Eds.), Soft Robotics: Trends, Applications and Challenges, Vol. 17 of Biosystems & Biorobotics, Springer, 2016.

[39] R. Ma, A. Dollar, Yale OpenHand project: Optimizing open-source hand designs for ease of fabrication and adoption, IEEE Robotics & Automation Magazine 24 (1) (2017) 32–40.

[40] G. P. Kontoudis, M. V. Liarokapis, A. G. Zisimatos, C. I. Mavrogiannis, K. J. Kyriakopoulos, Open-source, anthropomorphic, underactuated robot hands with a selectively lockable differential mechanism: Towards affordable prostheses, in: 2015 IEEE/RSJ International Conference on Intelligent Robots and Systems (IROS), Hamburg, Germany, 2015, p. 5.

[41] T. J. A. Buchholz, Bryan, S. A. Goldstein, Anthropometric data for describing the kinematics of the human hand, Ergonomics 35 (3) (1992) 261–273.

[42] L. Jiang, D. Sun, H. Liu, An inverse-kinematics table-based solution of a humanoid robot finger with nonlinearly coupled joints, IEEE/ASME Transactions on Mechatronics 14 (3) (2009) 273–281.

[43] H. Kawasaki, H. Shimomura, Y. Shimizu, Educational industrial complex development of an anthropomorphic robot hand 'Gifu hand', Advanced Robotics 15 (3) (2001) 357–363.

[44] T. Zhang, X. Q. Wang, L. Jiang, X. Wu, W. Feng, D. Zhou, H. Liu, Biomechatronic design and control of an anthropomorphic artificial hand for prosthetic applications, Robotica 34 (10) (2016) 2291–2308.

[45] H. Lipkin, A note on Denavit-Hartenberg notation in robotics, in: Proceedings of IDETC/CIE 2015, 2005, dETC2005-85460.

[46] M. W. Spong, S. Hutchinson, M. Vidyasagar, Robot modeling and control, John Wiley and Sons, Inc., Hoboken, NJ, 2006.

[47] T. Yoshikawa, Manipulability of robotic mechanisms, The International Journal of Robotics Research 4 (3) (1985) 3–9.

[48] D. A. Neumann, Kinesiology of the musculoskeletal system-e-book: foundations for rehabilitation, Elsevier Health Sciences, 2013.

[49] R. M. Gurbuz, Hulya, T. F. Nesrin., Measurement of active abduction of metacarpophalangeal joints via electronic digital incinometric technique, Italian journal of anatomy and embryology 9 (1).

[50] M. Nordin, e. Victor Hirsch Frankel, Basic biomechanics of the musculoskeletal system, Lippincott Williams & Wilkins, 2001.

[51] A. M. Cretu, P. Payeur, E. M. Petriu, Soft object deformation monitoring and learning for model-based robotic hand manipulation, IEEE Transactions on Systems, Man, and Cybernetics, Part B (Cybernetics) 42 (3) (2011) 740–753.

[52] S. Q. Ji, M. B. Huang, H. P. Huang, Robot intelligent grasp of unknown objects based on multisensor information, Sensors 19 (7) (2019) 1595.

[53] M. R. Cutkosky, On grasp choice, grasp models, and the design of hands for manufacturing tasks, IEEE Transactions on Robotics and Automation 5 (3) (1989) 269–279.

Appendix A. D-H parameters of the MCR-Hand III

In the tables, angles are in radian and lengths are in millimetres.

Table A.4: D-H parameters of the Thumb

i	α_{i-1}	a_{i-1}	d_i	θ_i
1	$\pi/2$	-20.62	0	0
2	0	0	30.25	θ_{11}
3	$-\pi/2$	-10.66	0	θ_{12}
4	$\pi/2$	44.2	0	θ_{13}
5	0	39.7	0	θ_{14}
6	0	21.2	0	0

Table A.5: D-H parameters of the index finger

i	α_{i-1}	a_{i-1}	d_i	θ_i
1	0	0	0	0.364
2	0	-30.07	0	$-\pi/2$
3	0	87.09	0	$-\pi/2-\theta_{21}$
4	$\pi/2$	0	0	θ_{22}
5	0	46.4	0	θ_{23}
6	0	33.2	0	θ_{24}
7	0	25.2	0	0

Table A.6: D-H parameters of the middle finger

i	α_{i-1}	a_{i-1}	d_i	θ_i
1	0	0	0	0.364
2	0	-4.07	0	$-\pi/2$
3	$\pi/2$	91.5	0	θ_{31}
4	0	54.4	0	θ_{32}
5	0	38.2.4	0	θ_{33}
6	0	28.2	0	0

Table A.7: D-H parameters of the ring finger

i	α_{i-1}	a_{i-1}	d_i	θ_i
1	0	0	0	0.209
2	$\pi/2$	20.13	0	θ_{41}
3	$-\pi/2$	10.24	0	0
4	0	72.64	0	$1.466+\theta_{42}$
5	$\pi/2$	0	0	θ_{43}
6	0	51.4	0	θ_{44}
7	0	38.2	0	θ_{45}
8	0	25.2	0	0

Table A.8: D-H parameters of the little finger

i	α_{i-1}	a_{i-1}	d_i	θ_i
1	0	0	0	0.209
2	$\pi/2$	20.13	0	θ_{51}
3	$-\pi/2$	33.78	0	0
4	0	87.63	0	$1.466+\theta_{52}$
5	$\pi/2$	0	0	θ_{53}
6	0	42.2	0	θ_{54}
7	0	29.2	0	θ_{55}
8	0	21.2	0	0